# SIMULATION OF TOTAL-COLUMN FOOTPRINTS WITH FLEXPART 11 FOR A REGIONAL INVERSE APPLICATION IN THE LUND UNIVERSITY MODULAR INVERSION ALGORITHM (LUMIA)

JOHANNA RISSBACHER

Master's thesis
2026:E66

LUND UNIVERSITY

Faculty of Science
Centre for Mathematical Sciences
Computational Science

CENTRUM SCIENTIARUM MATHEMATICARUM

# Simulering av atmosfärens totala koldioxids fotavtryck med FLEXPART 11 för tillämpning inom invers modellering i LUMIA

**Johanna Rissbacher**

Thesis supervisors: Marko Scholze, Yohanna Villalobos, Vishnu Thilakan Manaparambil

Date: July 7, 2026

# Abstract

Accurate estimations of regional $CO_2$ fluxes are essential for understanding the global carbon cycle and further mitigating climate change. Satellite-based retrievals of column-averaged carbon dioxide ($CO_2$) from the Orbiting Carbon Observatory 2 (OCO-2) offer a promising avenue for estimating carbon fluxes with atmospheric inversion systems, as they provide higher spatial resolution and observational density than traditional in situ networks. However, the large volume of satellite observations presents the challenge of how the data can be processed in order to make simulations computationally feasible.

In this study, total-column $CO_2$ retrievals from OCO-2 were used to simulate total-column footprints with the Lagrangian FLEXible Particle Dispersion Model (FLEXPART) v.11. To reduce computational costs, an adaptive grid cell averaging scheme was applied to the satellite observations prior to the footprint calculations. The precomputed footprints were then used to assimilate OCO-2 observations for January and August 2022 with the Lund University Modular Inversion Algorithm (LUMIA). The resulting posterior fluxes were validated against ground-based observations from the Integrated Carbon Observation System (ICOS), non-ICOS sites contained in the Observation Package (ObsPack) dataset and the Total Column Carbon Observatory Network (TCCON).

The results show that the OCO-2-derived posterior fluxes reduced both mean biases and root mean square error (RMSE) in simulated $CO_2$ concentrations at many validation sites across Europe. The inversion performance was notably better in August than in January, reflecting the stronger observational constraint associated with the higher density and spatial coverage of OCO-2 observations during summer. Sensitivity experiments investigating the temporal and spatial prior error covariance parameters indicated that a temporal correlation length of 30 days and a spatial correlation length of 100 km yielded the most effective configuration for OCO-2 observations, in terms of reducing posterior mean biases at the validation sites.

# Popular scientific summary

Climate change is largely driven by human activities such as the burning of fossil fuels, which release large amounts of carbon dioxide ($CO_2$) into the atmosphere. This additional $CO_2$ disrupts the Earth's natural carbon cycle by altering the balance between carbon sources and carbon sinks, such as forests and oceans, which absorb part of the emitted carbon. In particular, the future development of the land carbon sink remains uncertain under a changing climate, highlighting the need for accurate estimates of carbon fluxes.

One method used to estimate carbon fluxes is atmospheric inverse modeling. This approach combines atmospheric transport models with observations of $CO_2$ concentrations to improve prior estimates of carbon fluxes. The observations can originate either from ground-based measurement stations or from satellites. Ground-based stations provide highly accurate measurements at specific locations, whereas satellites measure the average $CO_2$ concentration throughout an entire air column, reaching from the Earth's surface to the top of the atmosphere. Hence, the resulting observation is a total-column measurement. Compared with the relatively sparse ground-based observation network in Europe, the Orbiting Carbon Observatory 2 (OCO-2) satellite provides much denser spatial coverage, enabling observations over large areas. However, satellite measurements depend on sunlight and are affected by clouds and aerosols, leading to lower data availability during winter months. As the ability to improve prior carbon flux estimates with atmospheric inverse systems is ultimately limited by observational density, using satellite-based observations is desirable.

The aim of this study was to extend the capabilities of the Lund University Modular Inversion Algorithm (LUMIA) to estimate carbon fluxes constrained by satellite-based $CO_2$ observations. Specifically, the current version of the atmospheric transport model (FLEXible PARTicle Dispersion Model - FLEXPART 11) used within LUMIA enables a simulation of the transport with total-column data, such as satellite observations. These transport simulations are also called total-column footprints. The scope of this project was to create the total-column footprints for LUMIA, which are needed to ultimately estimate the carbon fluxes constrained by observations. However, since satellites generate a very large number of observations, efficient processing methods are required to make the simulations computationally feasible. The inversion system ultimately produces estimates of carbon fluxes, which can then be converted into atmospheric $CO_2$ concentrations and compared with independent observations. This allows the evaluation of whether the optimized flux estimates improve the agreement between simulated and observed concentrations.

The results showed that the satellite-derived posterior fluxes reduced concentration biases at many validation sites across Europe. The performance of the inversion system was generally better during August, when observational coverage from OCO-2 was high, than during January, when the number of available satellite observations was substantially lower. Overall, this study demonstrates the potential of integrating satellite observations into regional atmospheric inversion systems, such as LUMIA, and explores the new capabilities of FLEXPART 11.

# Acknowledgements

I would like to greatly thank my supervisors, Marko, Yohanna, and Vishnu, for their guidance and support throughout this process. Further, I would like to thank my classmates and friends, who made every study break from the endless library sessions genuinely enjoyable. A special thank you to all of my roommates, who kept me motivated and cheered me on, especially in tough times. Last but not least, special thanks to my family for all their support.

# Contents

# Chapter 1

# Introduction

Climate change is driven by the accumulation of greenhouse gases in the atmosphere, among which carbon dioxide ($CO_2$) is predominant (Arias et al. 2021). It enters the atmosphere in large quantities by anthropogenic activities, which include mainly fossil fuel combustion, cement production and land use change (primarily deforestation). For the global carbon budget, Friedlingstein et al. (2026) estimates the fossil $CO_2$ emissions for the year 2024 to 10.3 $\pm$ 0.5 GtC $yr^{-1}$ and land-use change emissions to 1.3 $\pm$ 0.7 GtC $yr^{-1}$, resulting in total anthropogenic $CO_2$ emission of 11.6 $\pm$ 0.9 GtC $yr^{-1}$ (42.4 $\pm$ 3.2 $GtCO_2$ $yr^{-1}$). Further, this human-caused increase in atmospheric $CO_2$ amounts to an atmospheric growth rate of 7.9 $\pm$ 0.2 GtC $yr^{-1}$ (3.73 $\pm$ 0.1 ppm $yr^{-1}$), which is 2.2 GtC above the 2023 growth rate. The excess in atmospheric $CO_2$ is partly removed from the atmosphere by terrestrial (1.9 $\pm$ 1.1 GtC $yr^{-1}$) and oceanic (3.4 $\pm$ 0.4 GtC $yr^{-1}$) carbon sinks. However, summing the carbon sources and sinks yields a carbon budget imbalance of -1.7 GtC $yr^{-1}$, suggesting that the total sink or the atmospheric growth rate is strongly overestimated in 2024. Moreover, this indicates that the carbon cycle response to anthropogenic increases in atmospheric $CO_2$ concentrations is not fully understood and is inadequately captured by current model estimates.

According to the Sixth Assessment Report of the Intergovernmental Panel on Climate Change (IPCC) (Arias et al. 2021), increased carbon emissions have enhanced carbon uptake by oceanic and terrestrial ecosystems over the years. Yet, Arias et al. (2021) points out that despite this growing uptake, both sinks become less efficient at higher atmospheric $CO_2$ concentrations. This is driven by complex interactions among processes within ecosystems and the atmosphere. Under all emission scenarios, both the ocean and land sinks are predicted to stop growing in the second half of the 21st century. However, the evolution of the land carbon uptake remains considerably more uncertain due to a large spread in model results and incomplete process representation, which reduces confidence in projections of future land carbon sinks. This highlights the need for accurate estimations of land-atmosphere carbon exchange fluxes.

There are two general approaches for estimating surface-exchange carbon fluxes. Bottom-up approaches parametrize ecosystem processes, such as photosynthesis and respiration, and provide detailed estimates of the spatial and temporal carbon fluxes. However, since they cannot account for the full complexity of natural processes, they rely on parameterizations, which are not always accurate and can introduce substantial uncertainties in total fluxes from terrestrial ecosystems (Sitch et al. 2015).

On the other hand, top-down approaches such as inverse modeling infer changes in the uptake and release of atmospheric $CO_2$ (e.g., the Net Ecosystem Exchange (NEE)) from observed atmospheric concentrations. Thereby, large-scale direct measurements of atmospheric $CO_2$ provide means to link observed concentration changes to changes in their sources and sinks. In practice, atmospheric inverse modeling couples an atmospheric transport model, which establishes the relationship between tracer concentrations and fluxes, with an optimization algorithm. The optimization task involves finding the most likely set of fluxes that best matches the observations. This is carried out considering some prior constraints and associated uncertainties (Bayesian approach).

Bearing in mind that the total atmospheric concentration of $CO_2$ is very well known, atmospheric inversion methods can reliably estimate $CO_2$ fluxes at very large scales (Gurney et al. 2002). However, their sensitivity degrades at finer scales, ultimately limited by the density of observational coverage (e.g., Peylin et al. (2013)). In the context of the Paris Agreement, there is growing interest in higher-resolution, country-scale inversions, which would also enable independent validation of national emissions reporting. This shift from global to regional inversion systems is facilitated by the increasing availability of observations at regional scales (e.g., from the Integrated Carbon Observation System (ICOS)) and remote sensing products such as the Orbiting Carbon Observatory 2 (OCO-2) (Konovalov et al. 2025).

A realization of regional inversion systems is, e.g., the Lund University Modular Inversion Algorithm (LUMIA) (Monteil and Scholze 2021), FLEXINVERT (Thompson and Stohl 2014) and PYVAR-CHIMERE (Fortems-Cheiney et al. 2017). The underlying atmospheric transport models of these inversion systems can broadly be divided into Lagrangian and Eulerian models. Eulerian models represent the atmosphere through spatial discretizations of the surface and atmosphere into grid cells, whereas Lagrangian models follow trajectories of individual computational particles.

In the past decade, satellite missions like OCO-2 and the Tropospheric Monitoring Instrument (TROPOMI) aboard the European Copernicus Sentinel-5 Precursor (S5P) satellite have grown substantially. They can measure atmospheric column mixing ratios (e.g., $XCO_2$) with near-global coverage and a higher spatial sampling density than current in situ observation networks. Combined with improved measurement accuracy and increasing pixel resolution (Das et al. 2025), higher sampling density could provide valuable insights into the sinks and sources of tracers at regional scales (e.g., Connor et al. (2008)), making the use of satellite retrievals in atmospheric inversion systems increasingly attractive. However, the large number of observations per day has posed challenges in effectively integrating them into atmospheric transport models and inversion systems.

So far, satellite observations have mainly been used with Eulerian atmospheric transport models (e.g., Varon et al. (2023); Villalobos et al. (2021); Zhang et al. (2021)). Compared to Eulerian models, Lagrangian models exhibit less numerical diffusion and can accommodate arbitrary observation geometries, making them better suited to handle high-resolution data (Thompson et al. 2025). However, since the number of required model calculations scales with the number of observations, their application to satellite data has remained limited (e.g. Ganesan et al. (2017); Wu et al. (2018)). This makes the use of Lagrangian particle dispersion models (LPDMs) with satellite observations an attractive yet underexplored area of research.

In this study, data assimilation was performed using the Lund University Modular Inversion Algorithm (LUMIA). The underlying atmospheric transport model is the Lagrangian FLEXible PARTicle dispersion model (FLEXPART). To date, LUMIA has only assimilated in situ observations, making the extension to satellite observations a desirable advancement.

Bakels et al. (2024) show that with the recent advancements of FLEXPART 11, releasing particles across a column becomes possible. This is crucial for satellite-based observations, as they measure the contents of a tracer across an air column reaching from the surface to the top of the atmosphere. Hence, these total-column observations need to be represented accordingly in atmospheric transport models. With FLEXPART 11, the framework for using satellite observations in inversion systems is laid out. Nevertheless, the handling of satellite observations presents some challenges, namely the processing of a large number of observations and the proper distribution of particles across the column for the atmospheric transport model. Resulting from that, this project aimed to extend the capability of LUMIA by integrating total-column satellite retrievals. Given the scope of this work, the main focus of this thesis was to create total-column footprints, which are precomputed, as this is computationally more efficient with Lagrangian models. These footprints can then be used within LUMIA to assimilate data. After successful implementation, the entire setup is validated using total-column data from the Total Column Carbon Observatory Network (TCCON) Sussmann et al. (2025), in situ measurements from the Integrated Carbon Observatory System (ICOS) (ICOS Research Infrastructure 2018), as well as non-ICOS sites, contained in the Observation Package (ObsPack) dataset (Masarie et al. 2014). This gives rise to the following research questions:

1. How well do simulated $CO_2$ concentrations, using OCO-2 total-column retrievals and prior fluxes derived from land surface models, match OCO-2 observations?

2. To what extent are biases in OCO-2-derived posterior concentration fields reduced against TCCON column retrievals and ground-based in situ observations?

The remainder of this thesis is organized as follows. Section 2 provides a theoretical background on atmospheric inverse modeling and source–receptor relationships. Section 3 describes the methodology and datasets used in the study. Section 4 presents the results, which are discussed in section 5 and section 6 provides the main conclusions.

# Chapter 2

# Theoretical Background

## 2.1 LUMIA Inversion system

The Lund Modular Inversion Algorithm is a Bayesian regional inversion system. It was designed to consist of different modules that can be used independently of each other. An in-depth description of LUMIA is provided in Monteil and Scholze (2021); only a brief overview of the underlying techniques is given here.
In general, the objective of an atmospheric inversion is to find the most likely set of control variables that determine the atmospheric content and distribution of a tracer by assimilating observations of the tracer's occurrence in the atmosphere. In this project, the tracer is carbon dioxide ($CO_2$). The control variables governing the atmospheric $CO_2$ content are $CO_2$ fluxes between the atmosphere, the land surface and the ocean.
To link the observed concentrations ($y$) with the $CO_2$ fluxes (control vector $x$), a numerical model of atmospheric transport is used (eq. 2.1).

$$y + \epsilon_y = H(x + \epsilon_x) + \epsilon_H \tag{2.1}$$

H denotes the atmospheric transport model, along with any additional steps required to express y as a function of x, such as accounting for boundary conditions and non-optimized fluxes. $\epsilon$ represents the error terms, where $\epsilon_y$ is the observation error, $\epsilon_x$ the control vector error and $\epsilon_H$ the model error.
In this case, the atmospheric transport model is linear, which is why H(x) can be formulated as $\mathbf{H}x$, with $\mathbf{H}$ being the Jacobian of H. This raises the possibility of precomputing a Jacobian matrix instead of running a full transport model.
To solve equation 2.1 for x, a variational approach is adopted, where the goal is to find the control vector $x$ that minimizes the cost function $J(x)$. This is achieved by iteratively minimizing the mismatch between the model outputs and the observations (Chatterjee and Michalak 2013). Accordingly, the optimal control vector $\hat{x}$ is a statistical compromise between the deviation from the prior estimate ($x_b$) and the fit to the observations $y$. Mathematically, the cost function $J(x)$ is expressed as follows:

$$J(x) = \frac{1}{2}[(x - x_b)^T \mathbf{B}^{-1}(x - x_b)] + \frac{1}{2}[(\mathbf{H}x - y)^T \mathbf{R}^{-1}(\mathbf{H}x - y)] \tag{2.2}$$

where $\mathbf{B}$ is the prior error covariance matrix and $\mathbf{R}$ the observation error covariance matrix. They are means to weight the relative contribution of the departure of the prior control vector $x_b$ and observations $y$ to the cost function.

The observation error covariance matrix $\mathbf{R}$ accounts for the measurement uncertainties ($\epsilon_{obs}$) and the model error ($\epsilon_H$). The latter arises from the inability of the transport model to reproduce the observations perfectly, even if the true $CO_2$ fluxes were known. This model error cannot be formally quantified, as this would require knowledge of the true fluxes, which are the quantities being inferred. Due to that, realistic model error estimates are introduced.
The prior error covariance matrix $\mathbf{B}$ is constructed with the variances and covariances. Specifically, the covariance between control vector elements $x_1$ and $x_2$ at grid cells with coordinates $p_1 = (u_1, v_1, t_1)$ and $p_2 = (u_2, v_2, t_2)$ decays exponentially with time and space. Mathematically, this can be formulated as:

$$cov(x_1, x_2) = \sigma_{x_1}^2 \sigma_{x_2}^2 e^{-(d(p_1,p_2)/L_h)^2} e^{-|t_1-t_2|/L_t} \tag{2.3}$$

$\sigma_{x_1}^2$ and $\sigma_{x_2}^2$ describe the variances assigned to the prior fluxes; as these are challenging to determine, they are constructed based on plausible assumptions. $L_h$ and $L_t$ are the spatial and temporal correlation lengths that control the decay of correlations with the distance in space and time.
Thus, an inversion system combines an atmospheric transport model with an optimization algorithm and incorporates prior assumptions about the variable of interest, its uncertainties, and the uncertainties of the observations and the model.
LUMIA was originally developed using the Lagrangian FLEXible PARTicle dispersion model (FLEXPART) version 10.4 (Pisso et al. 2019) as its atmospheric transport model to then assimilate in situ observations. The atmospheric transport model establishes the relationship between fluxes and concentrations, commonly referred to as Source-Receptor Relationships (SRR, section 2.2).
For this project, the transport component was upgraded to FLEXPART v.11, which performs transport calculations directly in the native vertical coordinates of the European Center for Medium Range Weather Forecasts (ECMWF) Integrated Forecasting System (IFS) (Bakels et al. 2024).

### 2.1.1 Prior and posterior fluxes

The initial estimates of $CO_2$ fluxes before an optimization with the observations are called prior or a priori fluxes. In the inversion system LUMIA, they consist of four components, namely biosphere, anthropogenic, oceanic and biomass burning. The estimates either originate from different inventory databases or are derived from ecosystem bottom-up model simulations. When the most likely set of fluxes that fit the observations is found, the resultant fluxes are called posterior or a posteriori fluxes.

### 2.1.2 Forward run in LUMIA

As LUMIA consists of different modules, it is also possible to use LUMIA without performing an inversion, so without any fitting of the prior fluxes to the observations. This is also referred to as performing a forward run of LUMIA (Monteil and Scholze 2021).
A simulated $CO_2$ concentration $y_m^i$ consists of the "foreground" ($y_{fg}^i$) and "background" ($y_{bg}^i$) contributions (eq. 2.4).

$$y_m^i = y_{bg}^i + y_{fg}^i \tag{2.4}$$

As LUMIA is a regional inversion system, the regional transport in a limited domain is accounted for. To compare simulated $CO_2$ concentrations with observations, it is therefore necessary to also account for $CO_2$ transported into the domain by air masses originating from outside it. This contribution is represented by the background concentrations ($y^i_{bg}$) and is provided by global coarse-resolution transport models, such as the Tracer Model v.5 (TM5) (Huijnen et al. 2010), or can be acquired from the Copernicus Atmosphere Monitoring Service (CAMS) [1], which produces global atmospheric inversions.
The foreground contributions ($y^i_{fg}$) result from the scalar product of the pre-computed observation footprints ($K$) with FLEXPART 11 (described in section 2.2) and the surface fluxes ($f$) (eq. 2.5):

$$y^i_{fg} = \sum_i \sum_c \langle K_i, f_c \rangle \tag{2.5}$$

$K_i$ is a vector storing the emission sensitives of the observation $y_i$ and $f_c$ are the surface fluxes, $c$ indicates the different flux components as described in section 2.1.1.

## 2.2 Regional atmospheric transport model FLEXPART

The regional transport within LUMIA is handled by the Lagrangian FLEXible PARTicle dispersion model (FLEXPART 11) (Bakels et al. 2024). Generally, atmospheric transport models can be divided into Lagrangian and Eulerian models. In an Eulerian model, the surface and atmosphere are discretized and their inflows, outflows, transformation and deposition of tracers are described as a function of time. They are widely used in the inverse modeling community. However, they typically feature a relatively high level of numerical diffusion (e.g., Reithmeier and Sausen (2002)) and the tracer released is immediately mixed within the grid cell (Stohl et al. 2005). Further, the spatial resolution of the concentration fields is restricted by the grid spacing of the model.
In contrast to that, Lagrangian particle dispersion models (LPDMs) compute trajectories of computational particles (further denoted as particles) that describe the transport and diffusion of the tracers in the atmosphere, based on meteorological input data. The released particles are only a means to compute the trajectories and simulate the transport processes (Seibert and Frank 2004). Due to the independence of the computational grid, concentration fields can be produced with potentially infinitesimal spatial resolution at relatively low computational cost (Bakels et al. 2024).
LPDMs can establish a linear Source-Receptor Relationship (SRR) by either being run forward or backward in time. Only linear processes are considered, as standard LPDMs do not account for nonlinear chemical reactions and all other atmospheric transport processes are linear (advection, diffusion, convective mixing, dry and wet deposition and radioactive decay). A forward run can be described by releasing particles from a source region and simulating their downstream transport. In a backward run, particles are released, e.g., at an observation site (receptor), and their trajectories are integrated backward in time to identify potential upwind sources. The SSR can be depicted in a source-receptor matrix (M), whose entries $m_{il}$ are defined by equation 2.6:

$$m_{il} = \frac{y_l}{x_i} \tag{2.6}$$

[1] https://ads.atmosphere.copernicus.eu/datasets/cams-global-greenhouse-gas-inversion?tab=overview

where $y$ is a vector containing the receptors and $x$ is a vector with the sources. For gridded data, the indices $i$ (sources) and $l$ (receptors) each combine the temporal and spatial dimensions (Seibert and Frank 2004).
FLEXPART returns gridded model output, which is concentrations and deposition values in the forward run and emission sensitivities in the backward run. The output of the backward run can also be termed "footprint".

### 2.2.1 Source-receptor relationship for a point release

In order to perform an inversion, LUMIA uses precomputed footprints, driven by meteorological fields from the fifth generation of ECMWF's atmospheric reanalysis (ERA5) (Hersbach et al. 2020). LUMIA was originally developed to assimilate in situ observations, which are point observations. The observations originate from the Integrated Carbon Observatory System (ICOS) (ICOS Research Infrastructure 2018), which provides over 40 atmospheric measurement sites across 16 European countries. However, it should be noted that the distribution of measurement sites is uneven, with denser coverage in Western Europe and a sparser network in Eastern and Southern Europe.
Using in situ measurements with a Lagrangian atmospheric transport model corresponds to a point release of particles, as every measurement site has a designated latitude, longitude and height. Hence, in the calculations, particles are released at a specific location and height, and their trajectories are traced backward in time. To quantify the upstream surface fluxes influencing the receptor, emission sensitivities are estimated by aggregating the residence time of particles in grid cell $i$ within a defined surface-layer height. This can be formulated by the following expression:

$$H_i^{point} = \frac{1}{\rho_i}\frac{1}{P}\sum_{p=1} l_{p,i}\Delta t_{p,i} \tag{2.7}$$

where $l_{p,i}$ represents the transmission function for particle $p$, which is the fraction of mass staying in the particle. For reactive gases, the mass can change due to atmospheric chemistry, for $CO_2$, $l_{p,i}$ equals one. $\Delta t_{p,i}$ is the residence time of the particle in grid cell $i$, $\rho_i$ is the air density in grid cell i and $P$ is the amount of particles released (Seibert and Frank 2004)
A footprint for a point receptor (i.e., in situ observation) is visualized in figure 2.1, where the receptor is an in situ station in Karlsruhe (central Germany). The pattern depicted is very typical, with sensitivity high upwind of the receptor and then gradually fading out.

### 2.2.2 Source-receptor relationship for a total-column release

In order to use total-column observations in inversion systems, from e.g., satellite missions (OCO-2, O'Dell et al. (2018)) or the ground-based Total Column Carbon Observatory Network (TCCON, Wunch et al. (2011)), total-column footprints need to be simulated.
In general, total-column measurements are indirect measurements in which inverse methods are applied to retrieve a tracer's concentrations in a vertical column reaching from the ground up to the top of the atmosphere. This is based on prior constraints from radiance measurements by a spectrometer. Since retrieving the tracer concentration continuously at every atmospheric pressure level is not feasible, the atmosphere is instead represented by a discrete set of pressure levels (Connor et al. 2008). OCO-2 uses 20 pressure levels, while TCCON uses 51, from which the column-averaged dry-air mole fraction is derived.

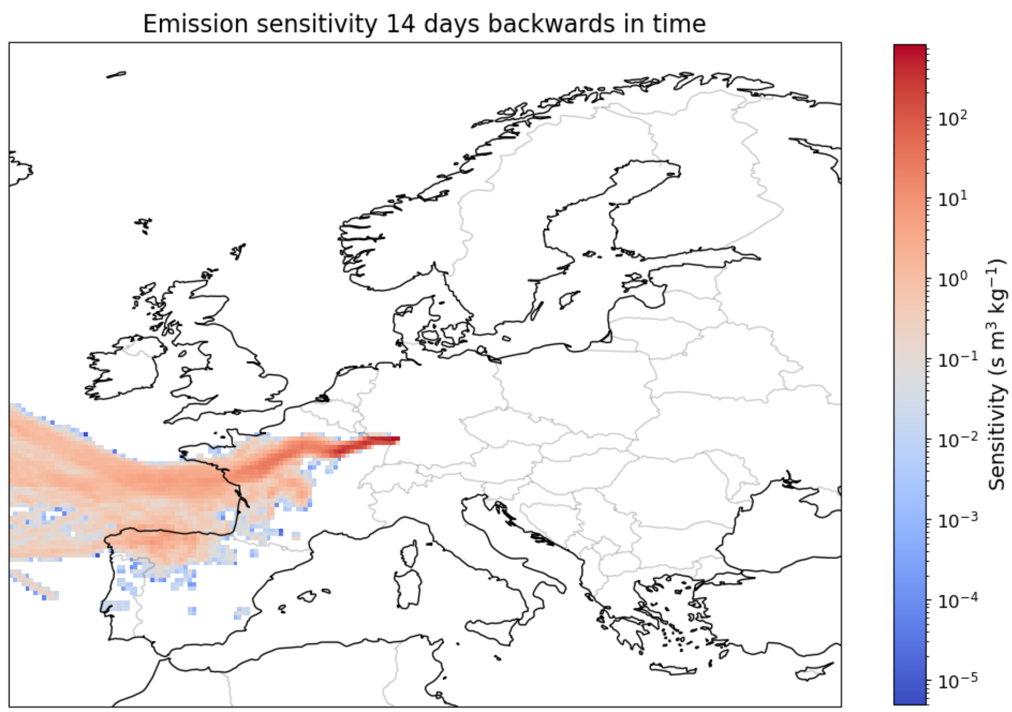


Figure 2.1: Footprint for a point release for the in situ site Karlsruhe on 2022-07-01 10:30, the emission sensitivities are marked in color.

**Averaging kernel and pressure weights**

For the calculation of a total-column footprint, the averaging kernel and the pressure weights are essential components of the implementation.
The averaging kernel is provided in datasets such as OCO-2 and TCCON at a discrete set of pressure levels. It describes the sensitivity of the total-column average to changes in the concentration within individual layers (Connor et al. 2008). Hence, a value of 1 in layer $n$ would imply that the change of concentration in layer $n$ leads to the same change of concentration in the total-column average. In an "ideal" case, the averaging kernel would equal 1 for every layer; however, for real retrievals, the values may be more or less than 1.
The pressure weighting term is related to the thickness of the pressure layer and captures how much atmospheric mass it represents. The pressure weights are either provided directly at the discrete pressure levels (e.g., for OCO-2) or calculated separately (e.g., for TCCON; see section 3.3.2).

**Calculation of a total-column footprint**

There are different approaches for calculating the SRR for a total-column retrieval. Previous studies (e.g., Ganesan et al. (2017)) calculated the column average SRR by calculating the SRR for every layer and forming the sum:

$$H^{col} = \sum_{n=1}^{N} a_n H_n w_n \tag{2.8}$$

where $H_n$ is the SRR, $a_n$ is the averaging kernel and $w_n$ the pressure weight for layer $n$.
For grid cell $i$, the SRR for layer $n$, for particles on a regular 3D grid, can be formulated as the following:

$$H_{i,n} = \frac{1}{P_n}\frac{1}{\rho_i}\sum_{p=1} l_{p,i,n}\Delta t_{p,i,n} \tag{2.9}$$

where $l_{p,i,n}$ expresses the transmission function for particle p, $\Delta t_{p,i,n}$ is the residence time of the particle in grid cell $i$ originating from layer $n$, $\rho_i$ is the air density in grid cell i and $P_n$ is the amount of particles released on layer $n$ (eq. 2.10) (Seibert and Frank 2004)

$$P_n = P a_n w_n \Leftrightarrow a_n w_n = \frac{P_n}{P} \tag{2.10}$$

Substituting eq. 2.9 into eq. 2.8 yields the following:

$$H_i^{col} = \frac{1}{\rho_i}\sum_{n=1}^{N} a_n w_n \left(\frac{1}{P_n}\sum_{p=1} l_{p,i,n}\Delta t_{p,i,n}\right) \tag{2.11}$$

However, this approach requires keeping track of the SRR for each layer in order to calculate the column SRR and is therefore computationally more demanding. Thompson et al. (2025) proposes a different approach, where the information of $a_n w_n$ is encoded by varying the particle density in each layer. The number of particles released is according to the averaging kernel and the pressure weights (eq. 2.10). Substituting eq. 2.10 into eq. 2.11 yields the following:

$$H_i^{col} = \frac{1}{\rho_i}\frac{1}{P}\sum_{n=1}^{N}\sum_{p=1} l_{p,i,n}\Delta t_{p,i,n} \Leftrightarrow H_i^{col} = \frac{1}{\rho_i}\frac{1}{P}\sum_{n=1}^{N} l_{p,i,n}\Delta t_{p,i,n} \tag{2.12}$$

The equivalence follows from the fact that summing over N layers and summing over all particles in the grid cell $i$ that originate from the N layers is equivalent. Equation 2.12 also shows that this method does not require calculating the SRR for every layer in order to obtain the total-column SRR. This is computationally advantageous compared to the approach presented before. Moreover, the varying amount of particles per layer ensures that particles originating from upper layers are more unlikely to reach the surface layer (Thompson et al. 2025).

With the current version of FLEXPART (v.11), more flexible particle inputs are available. This enables an efficient way of backward simulations of FLEXPART with satellite retrievals (Bakels et al. 2024). However, the use of satellite observations in inversion systems brings two main challenges with it (Thompson et al. 2025). Firstly, satellite missions provide an order of 10 000 to 100 000 retrievals globally per day, which makes simulations computationally demanding. Secondly, the geometry of the retrievals is not necessarily rectangular and is additionally rotated with respect to the meridians and parallels. As the standard release volume in FLEXPART is rectangular and aligned with the meridians and parallels, this needs to be handled correctly.

How to tackle these challenges and make simulations possible is further described in section 3.

# Chapter 3

# Methods

## 3.1 Preprocessing of Total-Column $CO_2$ Observations

In order to create total-column footprints and further integrate total-column observations into the inversion system, the total-column retrievals need to be handled accordingly.
Thompson et al. (2025) explains the fundamentals of implementing satellite retrievals in a Lagrangian particle dispersion model, specifically in FLEXPART 10.4. (Bakels et al. 2024) describes the new capabilities of FLEXPART 11. This includes the option to start a simulation with user-defined particle-release information, which enables the integration of satellite retrievals into FLEXPART 11.
As creating a total-column footprint for every observation (several thousand per day) would incur an infeasible computational cost, an efficient averaging scheme at a higher resolution is needed. This can be referred to as forming super-observation. To capture as much variability in the data as possible while averaging to higher resolutions, a variable grid cell size averaging routine was adapted. It is based on the standard deviation of the retrievals and is adapted from Thompson et al. (2025).

### 3.1.1 Satellite retrieval averaging routine

First, the domain (15°W, 33°N to 35°E, 73°N) is divided into grid cell boxes aligned with the parallels and meridians at the coarsest resolution. The resolution steps are defined by equation 3.1, where $d_{min}$ describes the finest grid cell resolution and $nsteps$ the number of resolution steps.

$$res_{steps} = d_{min} * 2^{nsteps-1} \tag{3.1}$$

Figure 3.1 shows a schematic graph of the adaptive grid cell division, going from a coarser resolution to a finer one. The black grid boxes display the domain grid cells aligned with the meridians and parallels, whereas the gray lines show a simplified satellite geometry and one polygon represents the satellite pixel of one retrieval. The red circles show the centroid of every satellite pixel. OCO-2 provides, among other variables, column-averaged concentrations of $CO_2$ or short $XCO_2$, which is one of the variables being averaged according to the following averaging scheme.
First, the adaptive grid is generated by assigning satellite pixels to domain grid cells according to their centroids. For each domain grid cell (e.g., orange grid cell in fig. 3.1), the standard

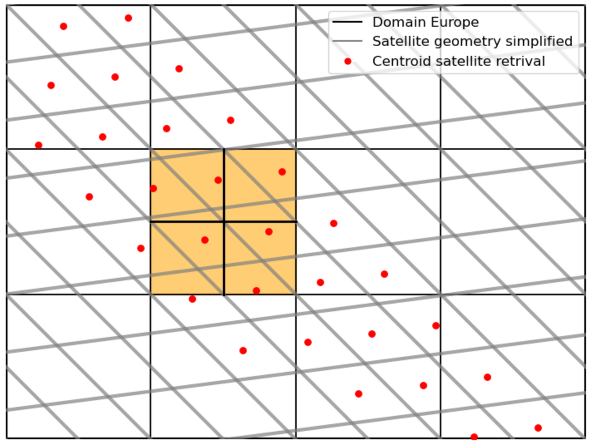


Figure 3.1: Schematic illustration of the grid cell subdivision scheme: black lines indicate the domain grid boxes, gray lines represent a simplified satellite footprint geometry, and red dots mark the centroids of the corresponding satellite retrievals. The orange grid box illustrates an example case in which the standard deviation of the retrievals within the grid box, exceeding a defined threshold, leads to the subdivision of the cell into quadrants.

deviation of all satellite retrievals that fall within the domain grid cell is computed. If the standard deviation exceeds a predefined threshold, the cell is divided into four equal subcells. Retrievals that lie outside ±2 standard deviations are determined as outliers and not considered later in the averaging. The same procedure is repeated for every resolution step. If there is a quarter where there are no retrievals, the grid cell is divided anyway to prevent creating a super-observation that is not fully represented by the retrievals.

Next, the area-weighted averages for each grid cell are formed. As the satellite pixels are distorted and rotated polygons, they overlap with different domain grid cells, which need to be taken into account when averaging. Another reason is that in reality, the satellite pixels have different sizes. Therefore, the retrievals should have a weighted contribution to the average of the grid cells.

To handle this, each satellite pixel is divided into a predefined number of sub-pixels. The centroid of each sub-pixel is then calculated, and depending on which domain grid box it falls within, its area is assigned to that grid box (fig. 3.2). The areas of all sub-pixels falling within a given grid cell are summed and multiplied by the $XCO_2$ concentration of the respective retrieval. The total area of all subpixels that fall into the domain grid cell is then used to weight the final concentration. Hence, the area-weighted average $XCO_2$ concentration ($\bar{c}$) of one domain grid cell is then given by the following equation:

$$\bar{c} = \frac{\sum_j \sum_i (s_{ij} * vmr_j)}{\sum_j \sum_i s_{ij}} \tag{3.2}$$

$j$ is the index of the satellite retrievals, $s_{ij}$ is the area of the ith subpixel and $vmr_j$ is the $XCO_2$ concentration of the jth retrieval that falls within the respective grid cell box.

Variables such as the averaging kernel, pressure weights, and observation time are aggregated using the same weighting scheme as that applied to $XCO_2$. With the averaging routine in place, the observations can be reduced significantly to a computationally more feasible amount

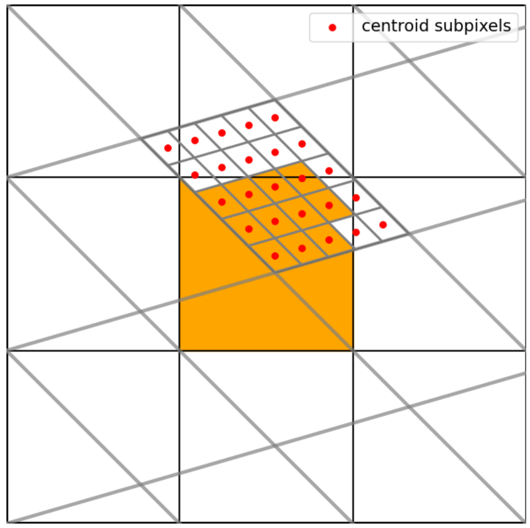


Figure 3.2: Schematic illustration of the area-weighted averaging routine: the black lines indicate the domain grid boxes, the gray lines represent a simplified footprint geometry, whereas the additional gray lines within one satellite footprint indicate the sub-pixel division and the red dots mark the centroids of the sub-pixels. The sub-pixels displayed in orange indicate that the centroid of the sub-pixel falls within the domain grid box, also marked in orange, and therefore their area contributes to the average.

of super-observations. Fig 3.3 shows the averaging routine applied to OCO-2 soundings from 14/07/2022. In this case, the resulting number of super-observations was two orders of magnitude smaller than the original number of observations. The different grid cell sizes that were used to form all the super-observations are 2°, 1° and 0.5°.

### 3.1.2 Particle column release with FLEXPART 11

As FLEXPART is a Lagrangian particle dispersion model, a defined number of particles needs to be released for every layer for every super-observation. To account for the varying sensitivity of each layer to the total-column average, the averaging kernel ($a_n$) and pressure weights ($pw_n$) are used to calculate the number of particles released on layer $n$ (eq. 3.3). Hence, a higher sensitivity results in a greater number of particles released in the respective layer. The pressure weighting term reflects how much atmospheric mass is captured by the pressure layer (Connor et al. 2008). For OCO-2, the pressure weights are also provided in the dataset; for TCCON they are calculated, as described in section 3.3.2.
To preserve the total amount of particles released, the raw weights ($raw\_w_n$) need to be normalized initially, as formulated in equation 3.4.

$$raw\_w_n = a_n * pw_n \tag{3.3}$$

$$w_n = \frac{raw\_w_n}{\sum_m raw\_w_m} \tag{3.4}$$

where $m$ denotes the summation index over all layers used in the denominator to normalize the raw weights. With the normalized weights ($w_n$), the number of particles released on layer

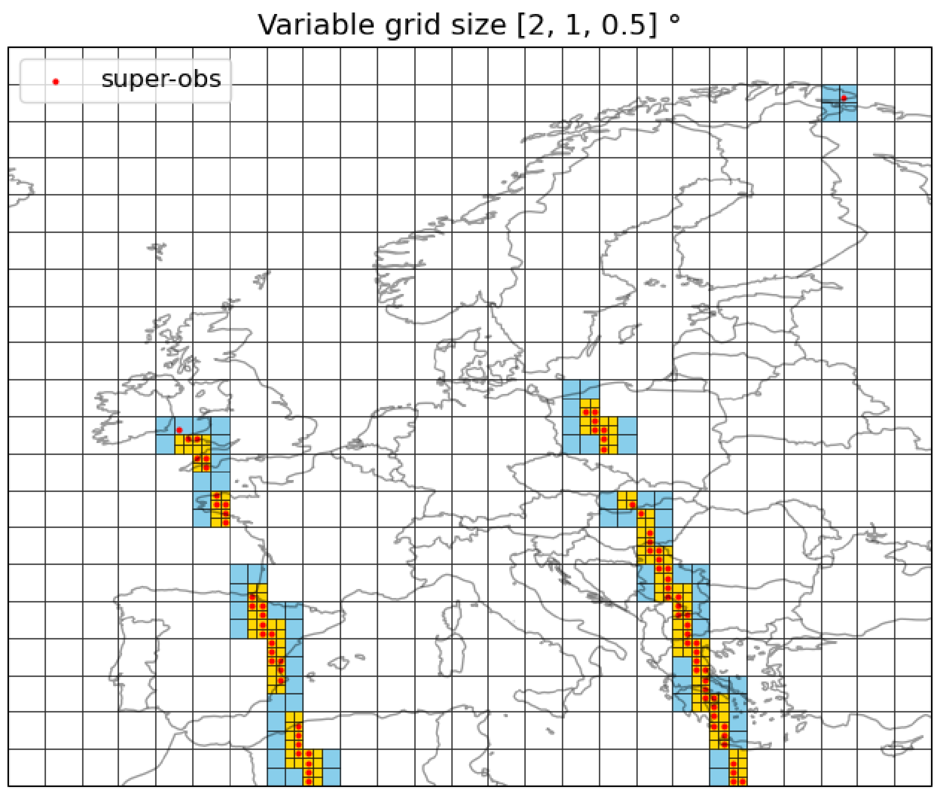


Figure 3.3: Variable grid size averaging routine applied to OCO-2 soundings from the 14/07/2022. The blue grid cells show a 1° resolution, whereas the yellow grid cells display a resolution of 0.5°. The red dots indicate the super-observations.

$n$ ($P_n$) can then be calculated from the total number of particles ($P$):

$$P_n = P * w_n \tag{3.5}$$

If the sum of particles per layer doesn't equal the total released particles, the remaining particles get assigned to the largest fractional remainder.
Apart from the particle release per layer, the initial particle positions, the initial particle mass, as well as the release time need to be provided in a NETCDF file for a user-defined particle release simulation in FLEXPART 11.
For each particle, the initial longitude and latitude are randomly and uniformly sampled within the grid box, and the initial height is randomly and uniformly sampled within the pressure bounds of the corresponding layer. In the surface layer, the lower and upper pressure bounds are identical and therefore all particles share the same initial height. The time of release of each particle comes from the area-weighted average of the super-observation. For the simulation, the release time needs to be set to seconds after the simulation start. The initial mass of each particle is defined such that the total particle mass per layer sums to one. Further instructions on how to start a simulation with user-defined particle information, including the exact structure of the NetCDF file, can be found in the FLEXPART 11 documentation[1]. This initialization file must be provided for every super-observation to then create the total-column footprints that are needed to perform forward runs and inversions with LUMIA.

## 3.2 Datasets

The main objective of this project was to integrate OCO-2 data into the inversion system, specifically to simulate total-column footprints with the atmospheric transport model FLEXPART 11. To create the total-column footprints, FLEXPART 11 utilizes meteorological data from the fifth generation of ECMWF's atmospheric reanalysis (ERA5) (Hersbach et al. 2020). For validation purposes, data from the Total Carbon Column Observing Network (TCCON) (Sussmann et al. 2025) as well as in situ observations from the Integrated Carbon Observatory System (ICOS) (ICOS Research Infrastructure 2018) were used. Additionally, in situ measurements from non-ICOS sites, provided in the Observation Package (ObsPack) dataset, are used to validate the posterior fluxes (Masarie et al. 2014).

### 3.2.1 OCO-2

The Orbiting Carbon Observatory 2 (OCO-2) is a satellite that takes space-based measurements of $CO_2$ on the sunlit hemisphere of the Earth. The three different viewing modes are nadir, glint and target. For this study, only land nadir observations (instrument points directly downward at the surface beneath the satellite) and land/ocean glint observations (the instrument follows the point of direct sunlight reflection from the Earth's surface) were included. The satellite crosses the equator around 13:30 Mean Local Time, which means it collects data above Europe at noon/early afternoon.
The measurement approach is based on spectrometers that measure the reflected sunlight from the Earth (Crisp 2008). $CO_2$ molecules absorb sunlight of a certain wavelength and therefore leave a fingerprint in the reflected sunlight that reaches the satellite. One of the challenges

[1] `https://flexpart.img.univie.ac.at/docs/configuration.html#satellites`

with this measurement is that the presence of clouds and optically thick aerosols, as well as uneven terrain, can block the light and lead to incomplete measurements of $XCO_2$. In order to reduce uncertainties, the satellite collects a large number of closely spaced samples. The acquired data is analyzed with remote sensing algorithms to obtain estimates of $XCO_2$.
The dataset used in this project (level 2, version 11.2) is freely available from the National Aeronautics and Space Administration (NASA) (OCO-2/OCO-3 Science Team et al. 2024). OCO-2 has a near-global coverage over a 16-day repeat cycle and a spatial resolution of 2.25 km x 1.3 km in nadir mode. The dimensions can vary by an order of $\pm 1$ km for other viewing modes. Moreover, Crisp et al. (2021) states a single-sounding precision in $XCO_2$ near 0.5 ppm and an accuracy within 1 ppm. Therefore, OCO-2 provides the data with the precision, accuracy and resolution needed to depict carbon sources and sinks on regional scales over the entire globe.

### 3.2.2 Meteorological Dataset for FLEXPART 11

As input data for the transport model FLEXPART, the fifth generation of ECMWF's atmospheric reanalysis (ERA5) (Hersbach et al. 2020) data was used. For the simulations, the reanalysis data were used at a 3-hourly temporal resolution and a spatial resolution of 0.25 ° × 0.25°.

### 3.2.3 Surface fluxes and background concentrations

The surface fluxes used within LUMIA are divided into four different components, namely biosphere, anthropogenic, oceanic and biomass burning emissions. All surface fluxes are obtained from different datasets and products, summarized in table 3.1.
The biosphere fluxes are acquired by simulations of the dynamical global vegetation model LPJ-GUESS (Smith et al. 2001). They are provided at a spatial resolution of 0.5° on an hourly temporal scale. In the selected inversion setup, the biosphere fluxes are the only component that is optimized and are therefore referred to as the prior fluxes.

| **Flux component** | **Data source** |
|---|---|
| Biosphere | LPJ-GUESS (Smith et al. 2001) |
| Anthropogenic | TNO GHGco v4 (Van der Gon 2023) |
| Biomass burning | CAMS-GFAS[2] |
| Oceanic | Mercator Ocean biogeochemical analysis[3] |

Table 3.1: Surface flux components used within LUMIA and their corresponding data sources

The anthropogenic emissions are obtained from the TNO GHGco v4 dataset with a resolution of 0.1° x 0.05° (Van der Gon 2023). Due to its well-characterized inventory-based nature, they are prescribed rather than optimized. The fire emissions are received from the CAMS-GFAS and the ocean fluxes are taken from the Mercator Ocean biogeochemical analysis. Both of these flux components are prescribed as well, because of the minimal impact on the net terrestrial $CO_2$ flux (Villalobos et al. 2025).

[2]https://ads.atmosphere.copernicus.eu/datasets/cams-global-fire-emissions-gfas
[3]https://doi.org/10.48670/moi00015

The background concentrations were obtained from the Copernicus Atmosphere Monitoring Service (CAMS) global dataset (v23r1) [4]

### 3.2.4 Validation datasets

#### TCCON

To validate the posterior fluxes, ground-based total-column data from the Total Column Carbon Observatory Network (TCCON), release GGG2020, are used (Sussmann et al. 2025). The network relies on ground-based Fourier transform spectrometers, which measure the absorption of direct sunlight. Meaning that, in contrast to OCO-2 observations, the sunlight only needs to penetrate the atmosphere once. In contrast to OCO-2 retrievals, they are less influenced by aerosols and land-surface variation (Wunch et al. 2011). TCCON provides data on 51 discrete pressure levels and at sufficient sunlight levels, measurements are provided every 2 minutes.

#### ICOS and ObsPack

The in situ observations for the validation are from the Integrated Carbon Observatory System (ICOS) (ICOS Research Infrastructure 2018) and the Observation Package (ObsPack) (Masarie et al. 2014), which is a product of ICOS and non-ICOS sites. ICOS provides over 40 atmospheric measurement stations in Europe, with a denser network in Western Europe and sparser observational sites in Eastern and Southern Europe. ObsPack delivers 14 additional non-ICOS sites across Europe. Again, the sites are mostly situated in Western and Central Europe.

## 3.3 Data assimilation with LUMIA

To test the simulation of the total-column footprints with OCO-2 and FLEXPART 11, data was assimilated with LUMIA and validated with in situ as well as with ground-based remote sensing products.

For the simulations with FLEXPART 11, 10000 particles (P) were released across the column and traced 14 days backward in time. The concentration averaging interval (LOUTAVER) was set to 3600 seconds and the model error to 4.5 ppm. The simulation months were January and August 2022. The observations used for the simulations were applied to a land-mask filter, where only soundings whose pixels cover a portion larger than 50% inland were considered. For the month of August, additional simulations were run using ocean and land soundings. This simulation month will therefore be referred to as August all_obs.

The total-column footprints were then used to run LUMIA forward and to solve the optimization task. The spatial correlation of the prior error covariance matrix was set to 500 km and the temporal correlation of the prior error covariance matrix was set to 7 days.

### 3.3.1 Sensitivity Experiments

As the previously stated correlation parameters (500 km, 7 days) were originally optimized for ICOS observations, it remains unclear whether OCO-2 observations require different correlation

[4] https://ads.atmosphere.copernicus.eu/datasets/cams-global-greenhouse-gas-inversion?tab=overview

parameters to achieve improved results, given their differing temporal and spatial resolutions. To investigate this further, sensitivity experiments were conducted.
The sensitivity experiments were limited to the month of August (land-soundings), as the higher observational density produced more promising results in terms of reducing the bias between the posterior fluxes and the observations. The tested cases are shown in table 3.2. Starting from the reference case, the parameters are varied one-at-a-time between a temporal correlation length of 7 and 30 days and a spatial correlation length of 100 and 500 km. Case 4 depicts a combination of reduced spatial and increased temporal correlation lengths.

| Case | Spatial correlation length [km] | Temporal correlation length [d] |
|---|---|---|
| 1 | 500 | 7 |
| 2 | 100 | 7 |
| 3 | 500 | 30 |
| 4 | 100 | 30 |

Table 3.2: Different cases of the sensitivity experiments

### 3.3.2 Validation of the posterior fluxes from OCO-2

Next, the posterior carbon fluxes need to be validated with independent data.
For point releases with ICOS and ObsPack, the inversion system LUMIA was already in place. In order to use the total-column data from TCCON, several preprocessing steps needed to be done.
Firstly, as TCCON provides measurements on a high temporal resolution, the observations were averaged to 10-minute intervals. To reduce computational cost and ensure consistent samples, as with OCO-2, one sample per day was collected at each observational site between 12:00 and 13:00. Specifically, the first available 10-minute average within this interval was selected. The time span was chosen because it is approximately the same time at which OCO-2 passes over Europe.
In order to run a simulation with the TCCON data with FLEXPART 11, the particle initialization files needed to be created. As for the OCO-2 data, the particles released per layer need to be calculated with the averaging kernel and the pressure weights (eq. 3.3, 3.4). However, the pressure weights are not provided in the TCCON dataset and therefore need to be calculated. As the concentrations are distributed at evenly spaced pressure intervals, the pressure weights are the same across layers except for the uppermost and bottommost layers.

$$pw_n = \begin{cases} \frac{1}{K-1} & 1 < n < 51 \\ \frac{1}{2(K-1)} & n \in \{1, 51\} \end{cases} \tag{3.6}$$

For the horizontal distribution of particles, the site's latitude and longitude are used. The variables height, mass and release time are defined following the same approach as for OCO-2. With the setup in place to validate the posterior fluxes from OCO-2 inversions with independent validation data, the first step is to simulate the footprints (ICOS and non-ICOS) or the total-column footprints (TCCON). LUMIA can then be run in forward mode (sect. 2.1.2), using the posterior fluxes from the OCO-2 inversion, to obtain modeled $CO_2$ concentrations, which can subsequently be compared with the observed concentrations. To quantitatively assess the agreement between the simulated and observed concentrations, the mean biases (eq. 3.7) and the root mean square error (RMSE, eq. 3.8) are calculated.

$$\text{Mean bias} = \frac{1}{N}\sum_{i=1}^{N}(obs_i - simulated_i) \tag{3.7}$$

$$RMSE = \sqrt{\frac{\sum_{i=1}^{N}(obs_i - simulated_i)^2}{N}} \tag{3.8}$$

# Chapter 4

# Results

## 4.1 Total-column footprint

After a successful implementation, total-column footprints can be simulated with FLEXPART 11. The footprints need to be created for every super-observation, one example of a total-column footprint from a super-observation at 2022-08-09, 12:11:29 in Central Germany, can be seen in figure 4.1. The sensitivities displayed here are gridded into a 0.25 x 0.25° raster. The pattern illustrated is very typical for footprints, with high sensitivity values in the vicinity of the receptor, which slowly fade out upstream.

## 4.2 Super-observations

To test the implementation of the total-column footprints, OCO-2 data for January and August 2022 were acquired. The purpose of choosing a winter and summer month was to test the influence of the observational density on the results of the inversions. Figure 4.2 shows the super-observations after applying the variable grid size scheme described in section 3.1.1. To visualize the observational density in the vicinity of the ICOS validation sites, the stations are displayed as magenta-colored triangles in fig. 4.2.

Super-observations were formed in greater numbers in August (1,615) than in January (662). The super-observations in January can mainly be found in the southern regions of Europe, with limited observational coverage in central Europe and almost no observations in Northern Europe. Contrary to that, the increased amount of observations in August leads to an increased amount of super-observations across all of Europe. The observations (glint and nadir mode) used to form the super-observations were applied to a land-fraction filter. Meaning that only soundings whose pixels prove a portion of larger than 50% inland, were used to form the super-observations. Without applying this land-filter, 2145 super-observations could be formed for August 2022. Including ocean soundings into an inversion was tested to see the influence of ocean soundings on the inland carbon uptake and release, especially for the coastal areas.

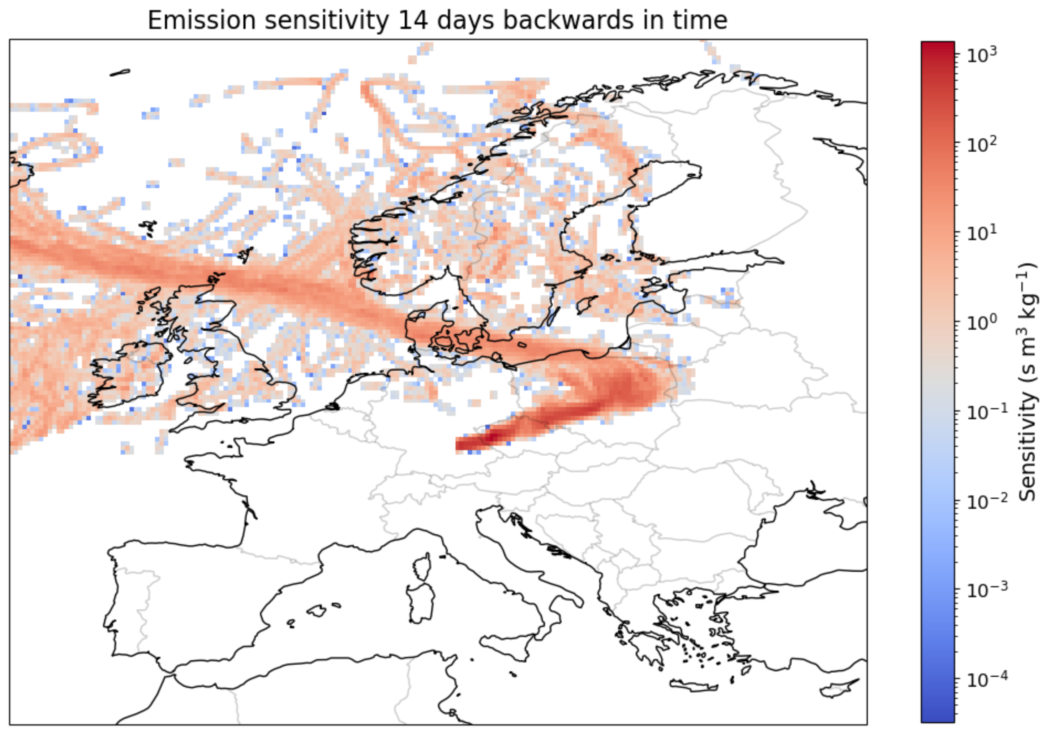


Figure 4.1: Total-column footprint for a super-observation at 2022-08-09 12:11:29, the emission sensitivities are displayed in color.

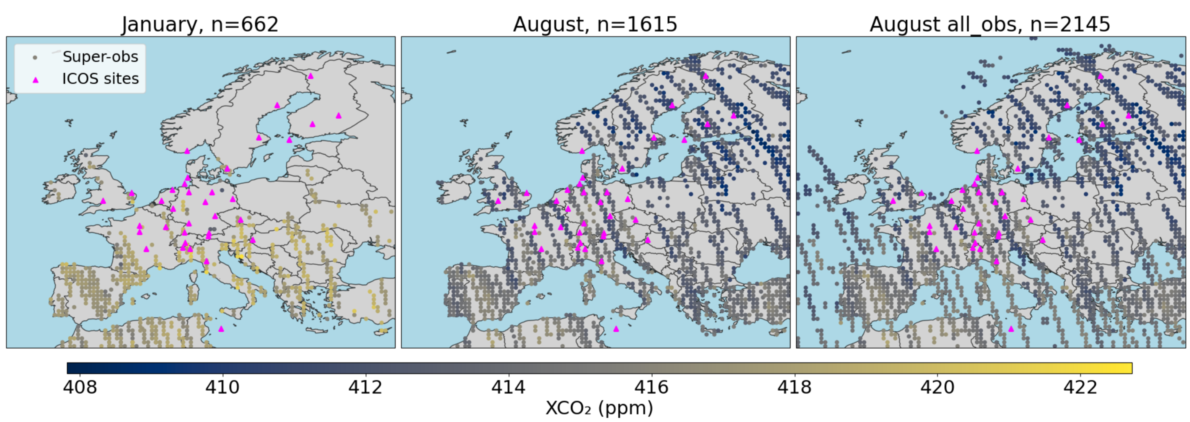


Figure 4.2: OCO-2 super-observations for January and August 2022. n indicates the number of super-observations, the circles show super-observations and the color of the respective super-observation corresponds to its $XCO_2$ concentration. The triangles display the ICOS sites.

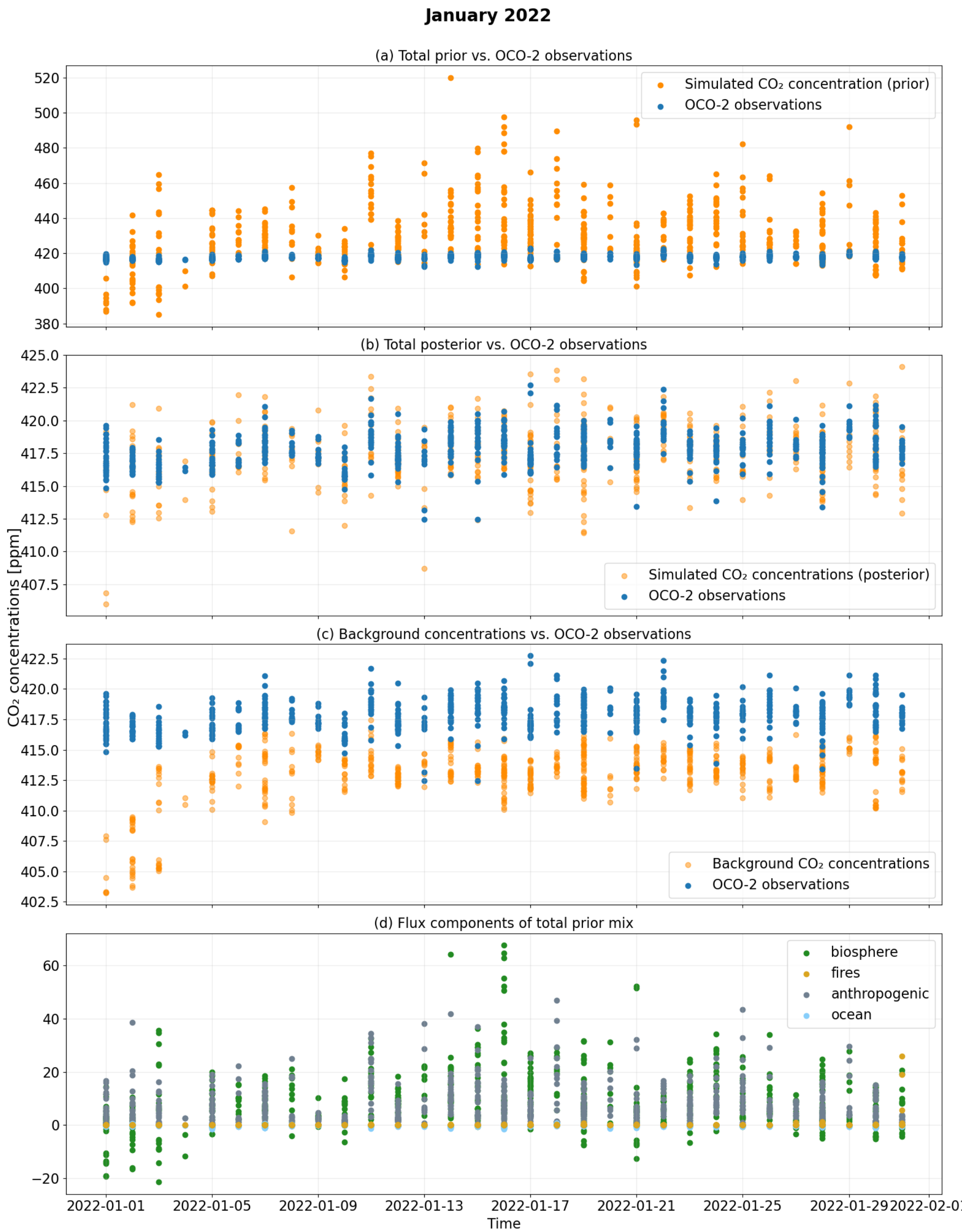


Figure 4.3: Comparison of simulated $CO_2$ concentrations (total prior (a), total posterior (b) and background concentration (c)) with OCO-2 satellite observations for January 2022; panel (d) shows the contribution of each flux component to the total prior.

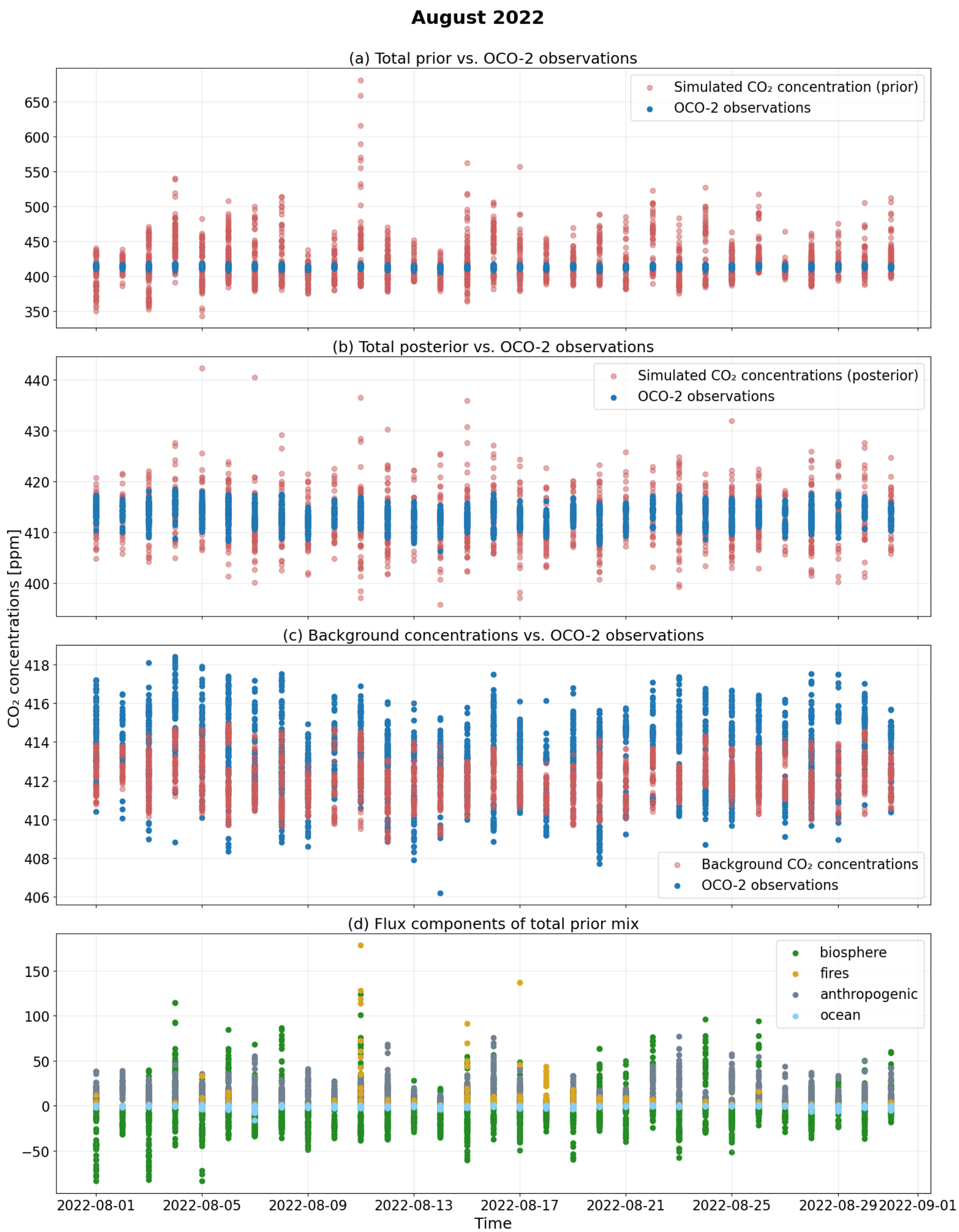


Figure 4.4: Comparison of simulated $CO_2$ concentrations (total prior (a), total posterior (b) and background concentration (c)) with OCO-2 satellite observations for August 2022; panel (d) shows the contribution of each flux component to the total prior.

## 4.3 Simulated $CO_2$ concentrations vs. OCO-2 observations with prior fluxes

As a first step, the $CO_2$ concentrations were simulated with the prior and posterior fluxes and then compared to the OCO-2 observations. Figure 4.3 (January) and figure 4.4 (August) display the simulated concentrations vs. the OCO-2 observations for all data points in the domain, visualized per day. The upper panel (a) shows the total prior, panel (b) shows simulations with the total posterior, while panel (c) only features the background concentrations of all data points in the domain for the respective month. Panel (d) shows the contributions of the single flux components of the total prior mix.

In both months, the simulated concentrations with the total prior (a) show much higher variability than the actual observed concentrations. Despite this, the observations still fall within the variability of the simulated concentrations, though they show a positive bias relative to the observations. Especially for January (fig. 4.3, a), the positive bias of the simulated concentrations is strongly pronounced.

Compared to the total prior, the background concentrations shown in panel (c) exhibit considerably less variability in both months and the simulated concentrations correspond closely to the observations. Again for January (fig. 4.3, b), the positive bias of the simulated concentrations is apparent.

For January, a larger spread of the flux components biosphere and anthropogenic can be depicted (fig. 4.3, d). In August, especially the flux component fire shows high values, indicating wild fire activity at some data points (fig. 4.4, d)

In contrast to the simulations driven by the prior fluxes, the posterior-flux simulations exhibit reduced variability and are in closer agreement with the observations. This improvement is evident in both January (fig. 4.3, b) and August (fig. 4.4, b).

## 4.4 Results of the OCO-2 data assimilation for January and August 2022

For the inversion setup, the spatial correlation of the prior error covariance matrix was set to 500 km and the temporal correlation of the prior error covariance matrix to 7 days. This is the same setup used previously for data assimilation of in situ observations within LUMIA.

Figure 4.3 (b), and 4.4 (b), shows the time series of simulated $CO_2$ concentrations, with OCO-2-derived posterior fluxes, compared to OCO-2 observations.

Figure 4.5 shows a spatial visualization of the biosphere flux. The left column displays the prior flux estimate originating from LPJ-GUESS, the middle column visualizes the posterior flux when assimilating ICOS observations and the right column exhibits the posterior flux, when assimilating OCO-2 observations. It can be seen that the prior for January shows a carbon release for most parts of Europe, with a stronger magnitude in Western Europe and a smaller magnitude in Northern and Eastern Europe. Both the ICOS posterior fluxes and the OCO-2 posterior fluxes show a carbon uptake in the region of the Benelux states and the southern parts of the British Isles. For the central and eastern parts of Europe, the ICOS posterior fluxes and OCO-2 posterior fluxes do not agree. While the ICOS posterior shows a carbon release, the OCO-2 posterior depicts a carbon uptake. However, these regions are characterized by a lower observational density of OCO-2 in January. Hence, the observational

constraints on fluxes in these regions are weaker, whereas especially Central Europe is better constrained by ICOS observations in January.
For August, the ICOS and OCO-2 posterior fluxes agree in the regions of the Benelux states, parts of western Germany and in northern Italy, showing a carbon sink. The prior flux also displays a carbon sink in the region of the Benelux states, however less pronounced. While the prior and the ICOS posterior fluxes depict large parts of Spain and Portugal to be a carbon source, the posterior fluxes from OCO-2 disagrees mostly, only displaying a smaller source in the north of Spain. When comparing the OCO-2 posterior of August and August all_obs the spatial image looks very similar. For August, using all observations, a slightly less pronounced carbon release is indicated in the south of France as well as in the north of Spain, compared to the posterior flux from August using the land-filter.
Figures 4.6, 4.7, 4.8, 4.9 show OCO-2 observations within 500 km of the ICOS sites for August 2022. Due to the lack of OCO-2 observations in the very close vicinity of the ICOS measurements ($\leq$ 100 km), a 500 km radius was chosen. Comparing these observations with the corresponding ICOS measurements reveals a consistent pattern across all stations. The OCO-2 observations vary less over time, while the ICOS measurements show larger fluctuations in $CO_2$ concentrations, reflecting their sensitivity to local-scale variability. Additional comparisons between OCO-2 observations and ICOS measurements within a 200 km radius are provided in Appendix 7

### 4.4.1 Validation with ICOS observations

To validate the posterior fluxes obtained from the inversion using OCO-2 super-observations, ICOS observations are utilized. Thereby, the concentrations were simulated using the prior (from LPJ-GUESS) and the posterior fluxes from the OCO-2 inversion. Owing to that, the mean biases will be from here on termed prior mean bias, if the prior fluxes were used to simulate the concentrations and posterior mean bias, if the posterior fluxes were used for the simulation of the concentrations. Moreover, the prior mix ratios will be referred to as prior concentrations for simplicity.
In order to compare the prior and posterior mean biases of the single stations in more detail, the stations were grouped in Northern, Eastern/Central, Southern and Western Europe. The division can be seen in figure 4.10. The station PRS in northern Italy only provided data for January. Figure 4.11 shows the mean biases that were calculated across the stations for January. The green shaded areas mark the stations, where the posterior flux reduced the mean bias in concentrations to the observations. On the x-axis, the station codes are listed, which are spatially plotted in figure 4.13. Stations marked in green exhibit a reduced mean bias with the posterior fluxes; stations marked in magenta did not improve compared to the prior. A full list of station names and station codes can be found in the Appendix 7.
Comparing figure 4.11 and 4.12 depicts that there are fewer stations with a reduced prior bias in January than in August, which is related to the differences in observational density. Further, the overall magnitude of the posterior mean biases is higher in January, with values ranging up to around $\pm$20 ppm. In contrast to that, the sites in August show a smaller magnitude of mean biases (around $\pm$10 ppm) with the posterior fluxes. For January, the stations in Northern Europe (fig. 4.11, a) reached a slight bias improvement with the posterior flux. However, the mean bias for these stations, when using the prior fluxes, was already close to zero. The stations in Central and Eastern Europe (fig. 4.11, c) reveal posterior biases around

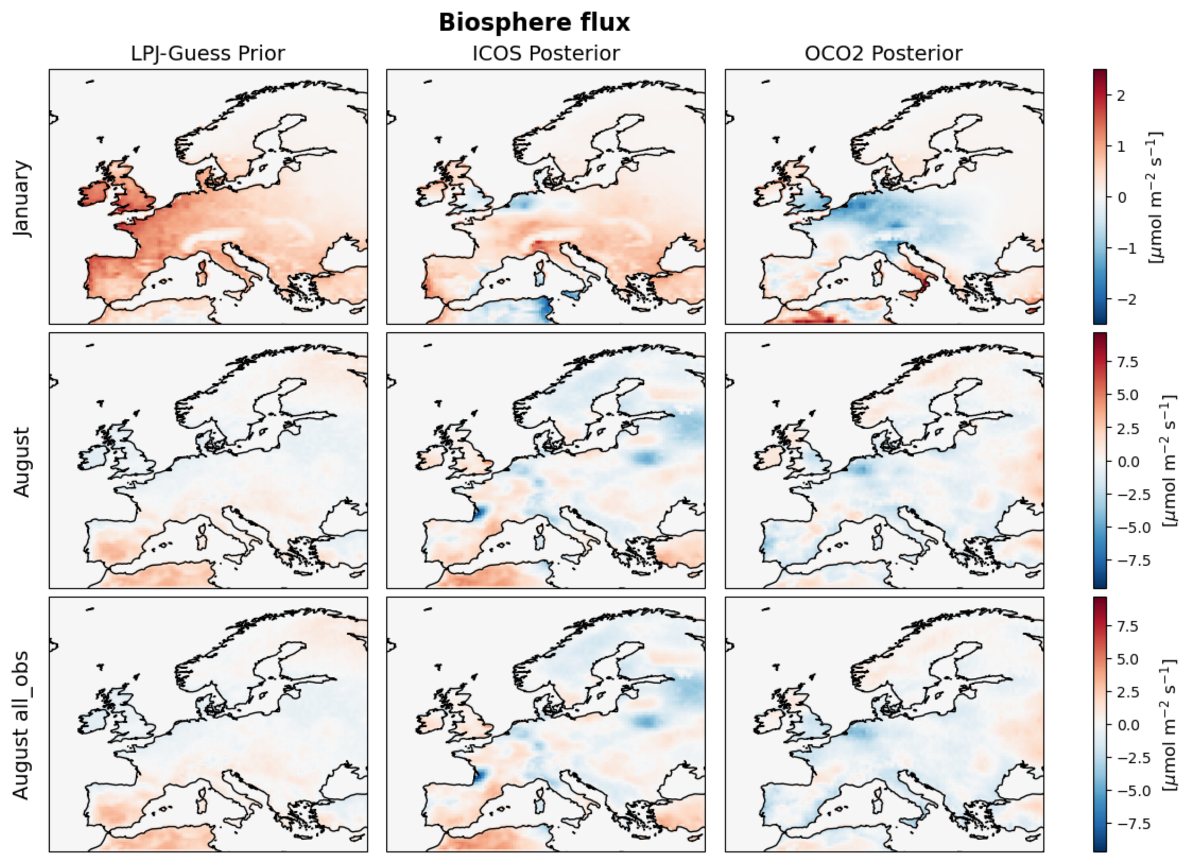


Figure 4.5: Spatial comparison of the prior fluxes from LPJ-GUESS to the ICOS and OCO-2-derived posterior fluxes, for the months January, August and August all_obs.

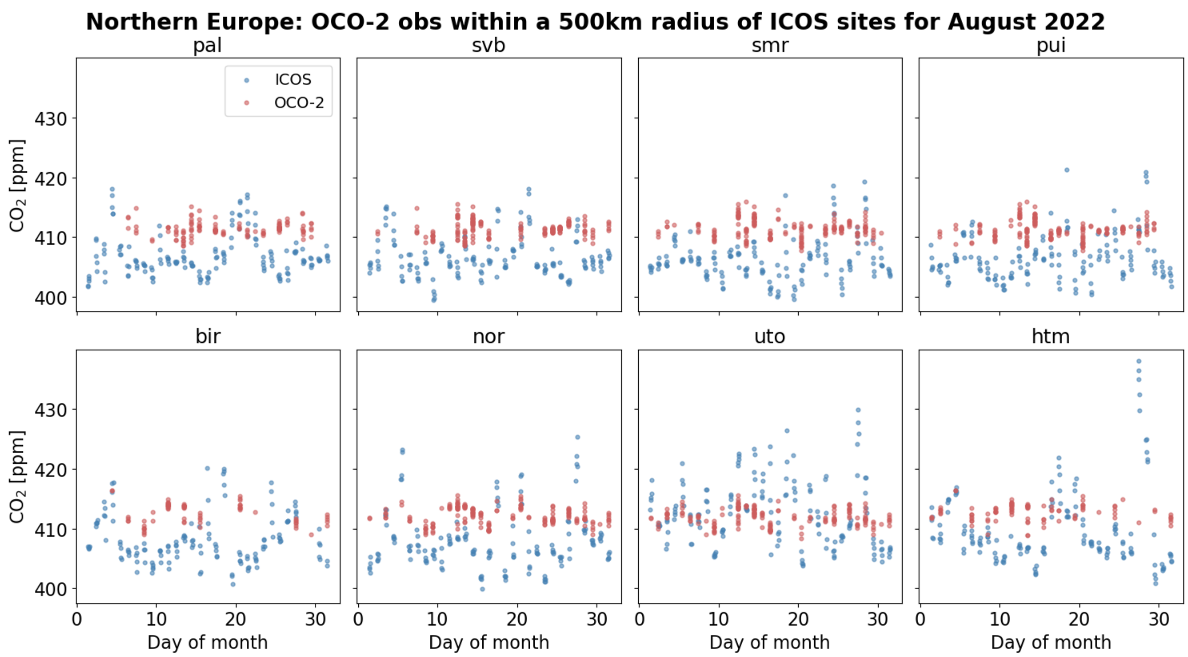


Figure 4.6: ICOS observations (blue) and OCO-2 observations (red) within 500 km of the respective ICOS site, displayed are the sites in Northern Europe for August 2022.

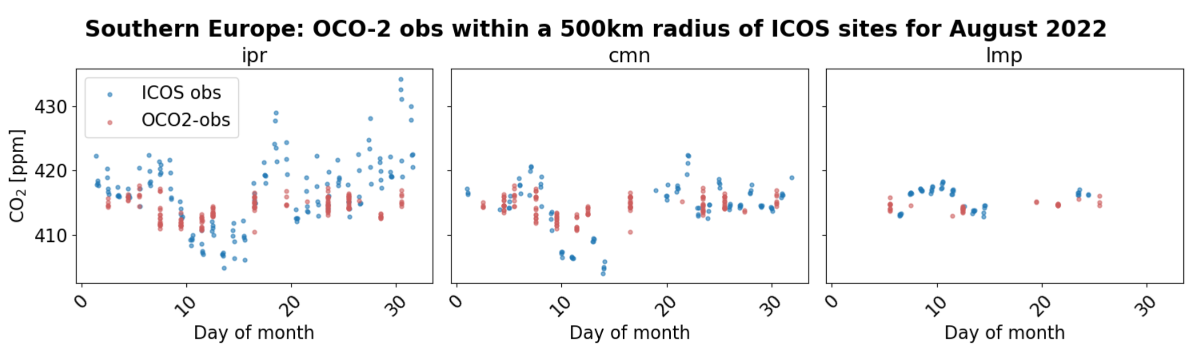


Figure 4.7: ICOS observations (blue) and OCO-2 observations (red) within 500 km of the respective ICOS site, displayed are the sites in Southern Europe for August 2022.

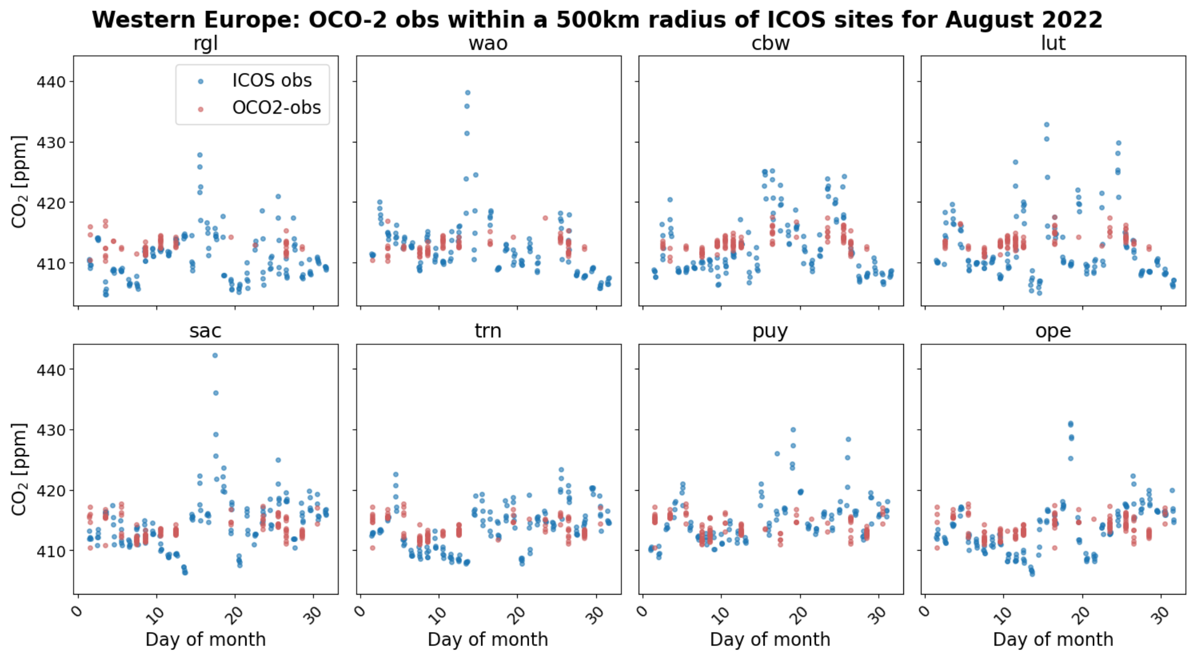


Figure 4.8: ICOS observations (blue) and OCO-2 observations (red) within 500 km of the respective ICOS site, displayed are the sites in Western Europe for August 2022.

10 ppm and higher for January. Further, the station WAO at the coast of England (fig. 4.11, d) achieved a mean bias improvement with the inversion, whereas in August (with and without ocean soundings), the posterior mean bias is above 8 ppm for that station.
Figure 4.13 shows, overall, the bias improvements in August are greater than in January. This can primarily be seen in Central Europe, where more OCO-2 soundings are available, e.g., across Germany. As seen in figure 4.12, the station IPR (Italy) in particular shows a large improvement in mean bias, with a prior mean bias of -9.26 ppm and a posterior mean bias of -1.42 ppm. In contrast to January, the inversion slightly improved the mean bias for the station HTM but failed to improve mean biases at the other northern European station (fig. 4.12, a), or at the stations WAO and RGL in England (fig. 4.12, d).
Comparing August and August all_obs the coastal station RGL accomplished a mean bias improvement with the inversion. As illustrated in figure 4.14 with an orange marker, the stations TRN and OPE were negatively influenced by including the ocean glint soundings into the data assimilation. After the inversion with all observations in August, these stations show no mean bias improvement anymore. However, the prior and posterior mean biases are of similar magnitude (fig. 4.12 c, d).

### 4.4.2 RMSE

In January, the overall largest RMSE in concentrations (above 20ppm) from the prior as well as the posterior flux can be seen at the mountain site IPR (fig. 4.15, b). Compared to the other regions in Europe, the northern sites show lower values in RMSE concentration when using prior or posterior fluxes (fig. 4.15, a). Figure 4.15 c depicts a large RMSE (22.03 ppm) for the station KIT in Germany, resulting from the posterior fluxes. For the stations TOH, LIN,

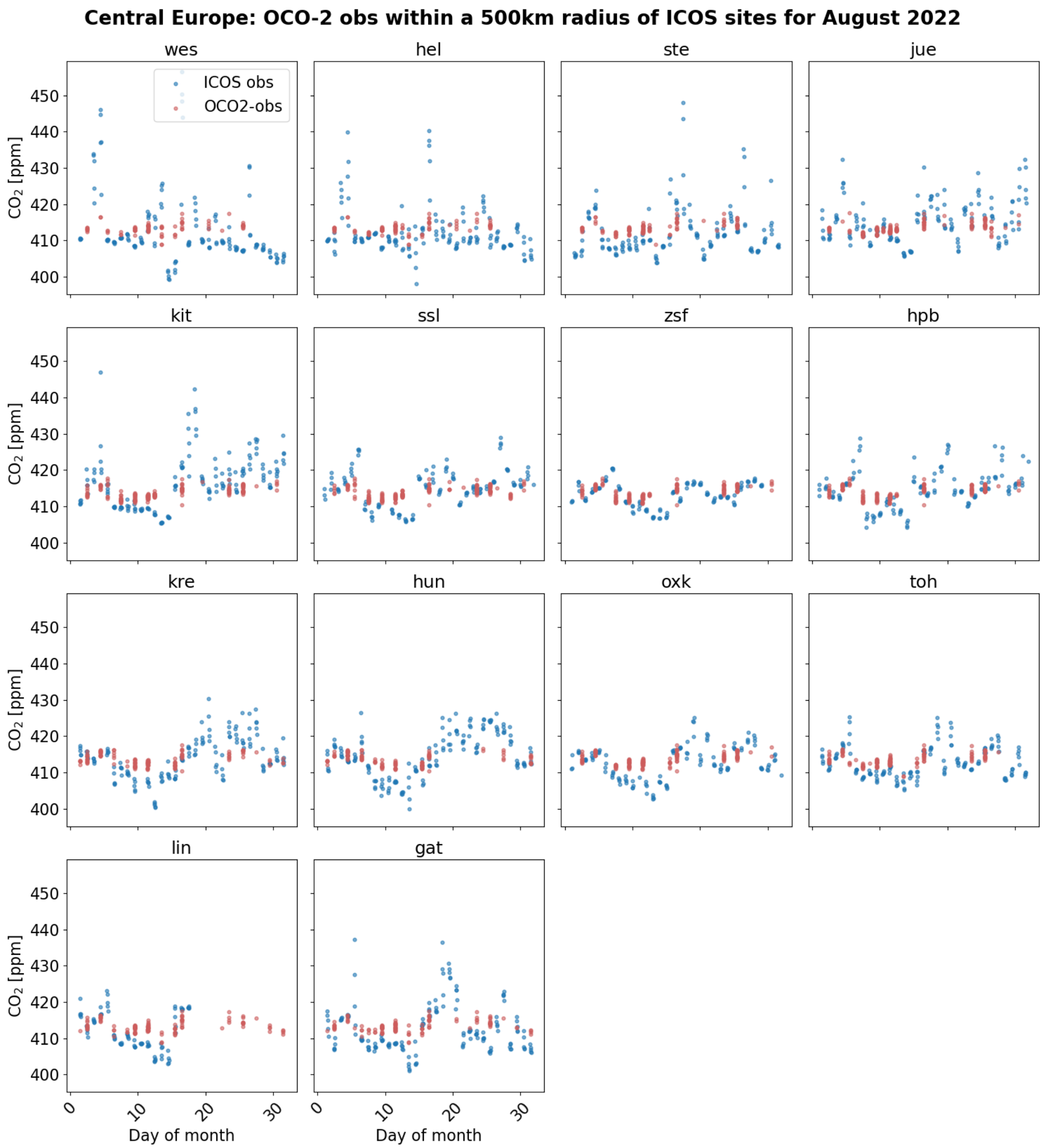


Figure 4.9: ICOS observations (blue) and OCO-2 observations (red) within 500 km of the respective ICOS site, displayed are the sites in Central/Eastern Europe for August 2022.

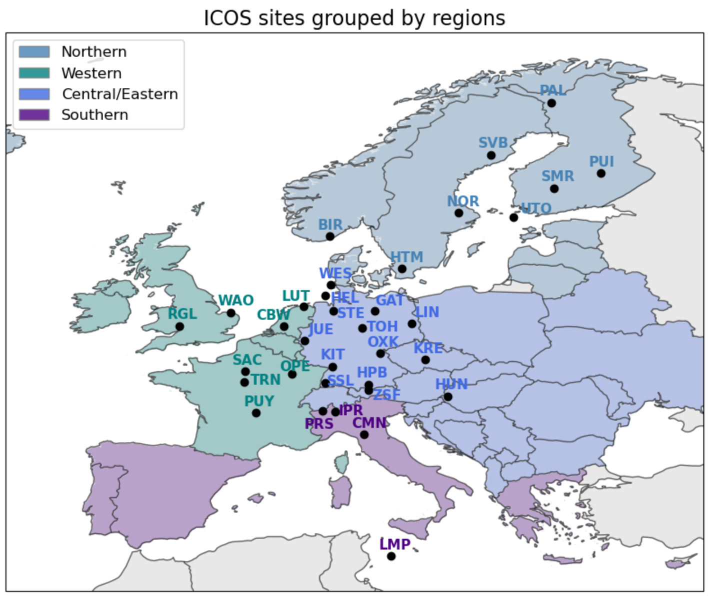


Figure 4.10: Locations of the ICOS atmospheric validation stations and their grouping into Northern (lightblue), Central/Eastern (blue), Southern (purple) and Western Europe (green)

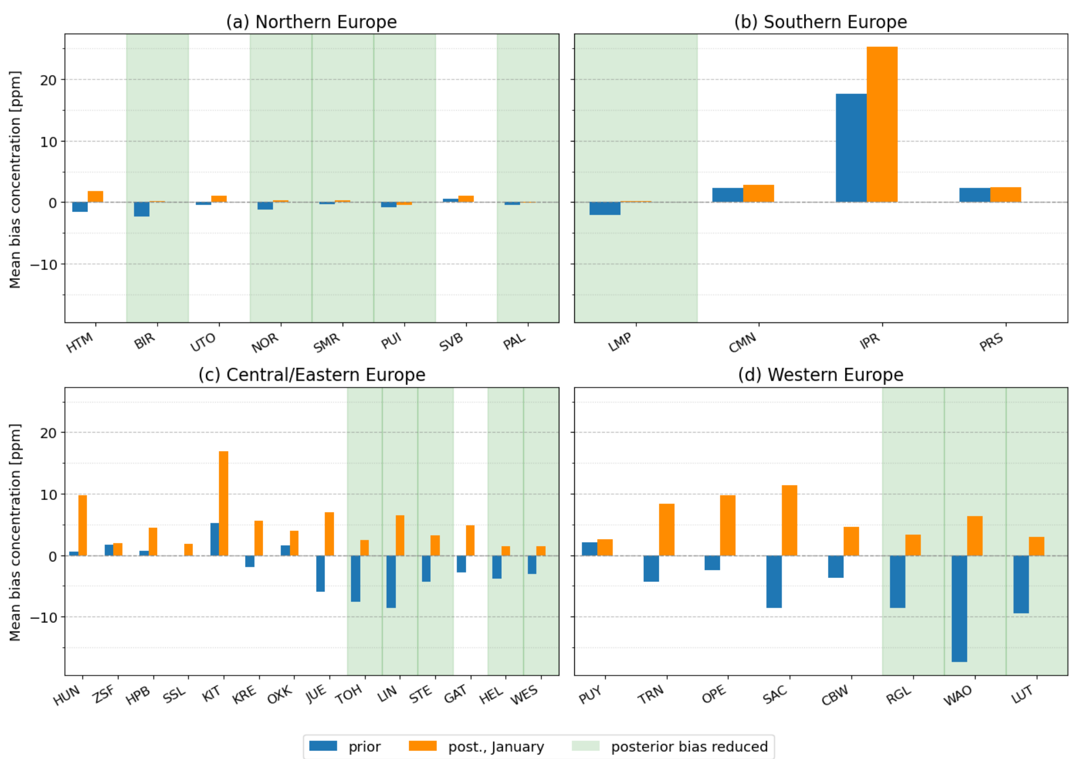


Figure 4.11: Mean biases in concentrations with the prior fluxes (blue) and the posterior fluxes (orange) for January 2022. The green shaded areas show an improvement of the posterior mean bias relative to the prior mean bias. The sites are grouped by region across Europe.

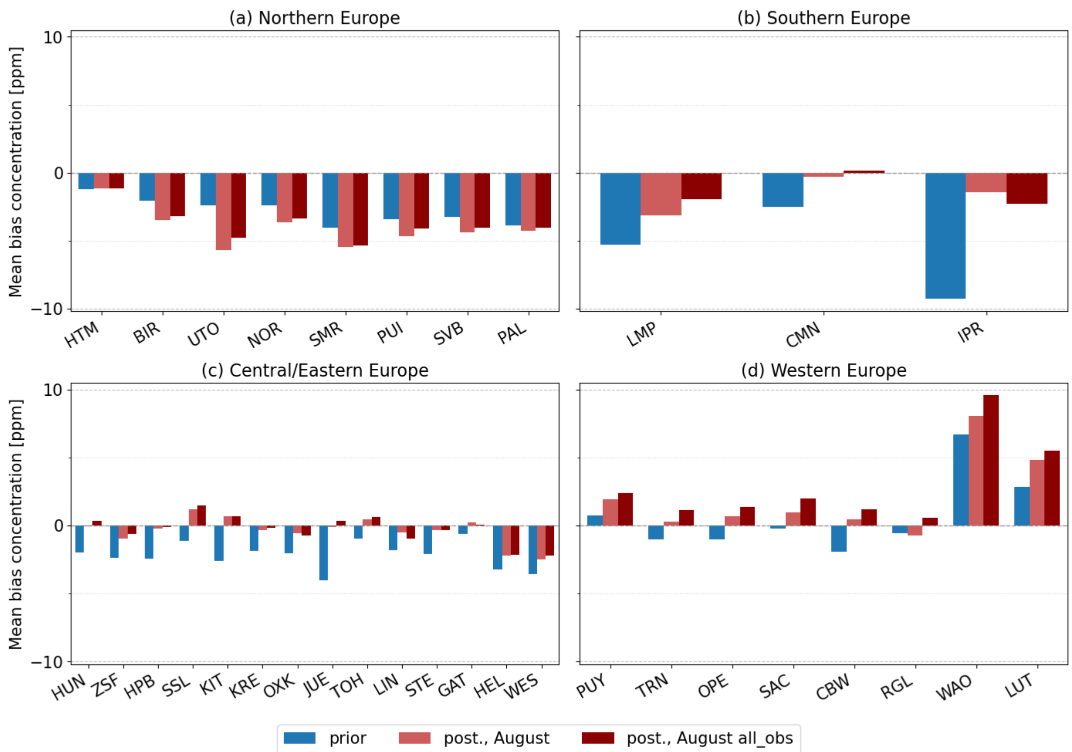


Figure 4.12: Mean biases in concentrations with the prior fluxes (blue) and the posterior fluxes for August (light red) and August all_obs (dark red) 2022. The sites are grouped by region across Europe.

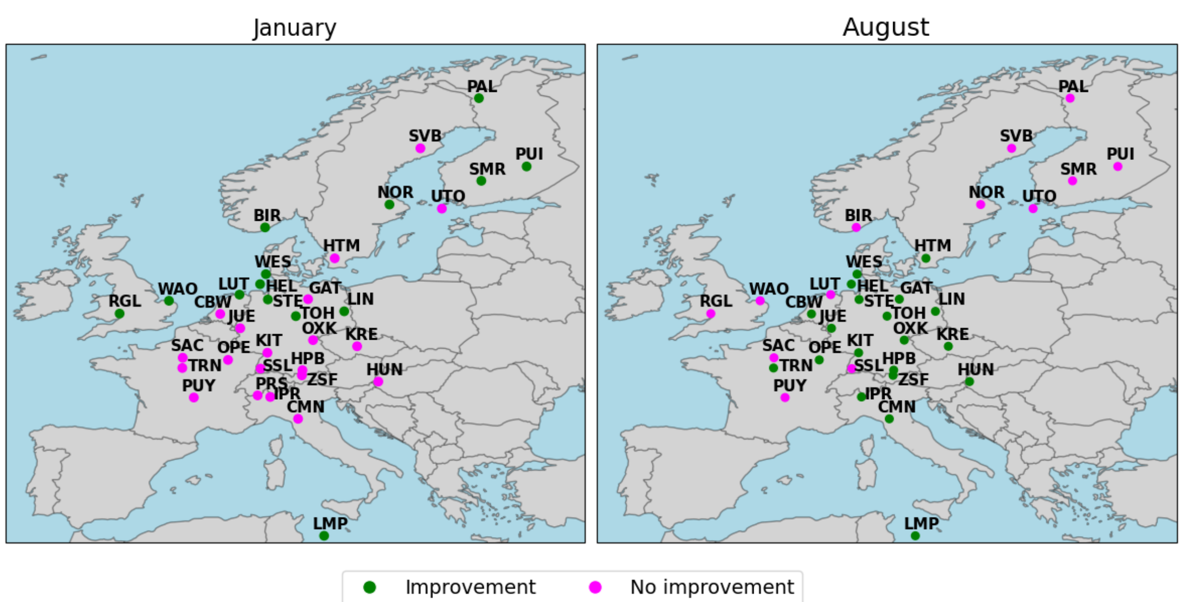


Figure 4.13: Spatial distribution of ICOS sites showing a mean bias improvement (green) and no improvement (magenta) for inversions in January (left) and August (right).

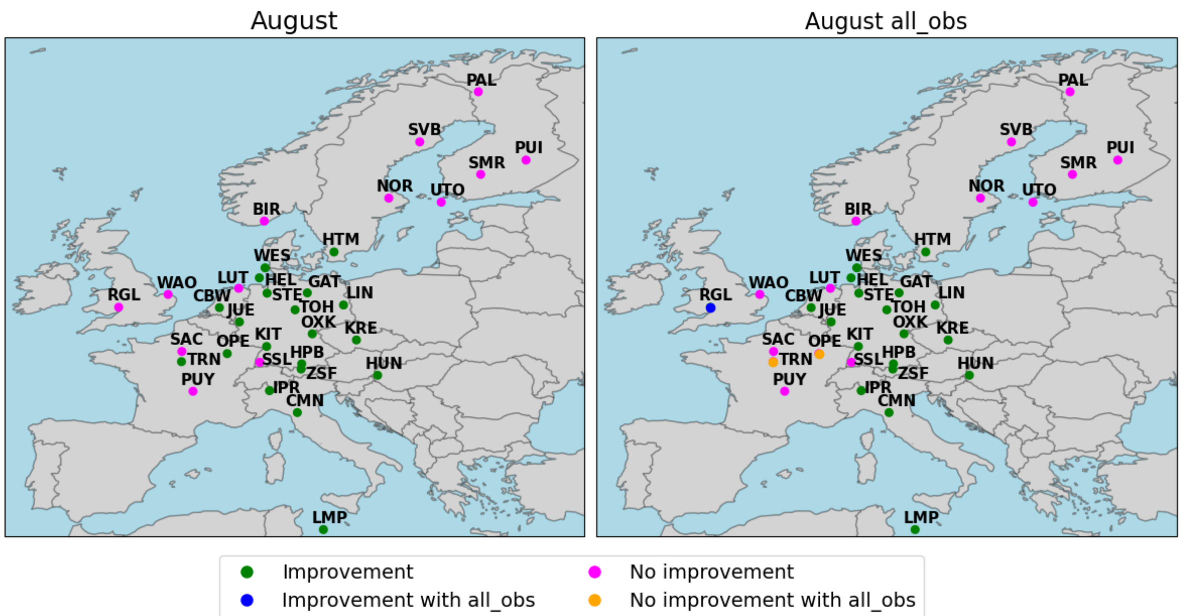


Figure 4.14: Spatial distribution of ICOS sites showing mean bias improvement (green) and no improvement (magenta) for two August inversions using land-only versus all observations (land and ocean). Navy markers indicate stations newly improved when ocean soundings are included; orange markers indicate stations that are not improved anymore when including all observations.


Figure 4.15: RMSE concentrations using the prior fluxes (blue) and posterior fluxes (orange) for January 2022. The sites are grouped by region across Europe.

HEL and WES, which are all located in Northern Germany, the RMSE was reduced using the posterior fluxes. The site SSL also achieved a reduced RMSE with the posterior flux, however only slightly less than the RMSE from the prior flux. For sites in Western Europe (fig. 4.15, d), the sites SAC and the two coastal sites LUT and WAO show high values in RMSE with the prior fluxes (above 15 ppm). For the stations WAO and LUT, the RMSE could be reduced to below 10 ppm with the posterior fluxes, whereas the RMSE for SAC even exceeded the prior RMSE.

Figure 4.16 displays the RMSE in concentration at the sites in Europe, using the prior fluxes and posterior fluxes from the inversions of August and August all_obs. Again, the mountain site IPR showed the highest RMSE from the prior fluxes, which could be reduced with both posterior fluxes from the August inversions (fig. 4.16, b). For all stations in Northern Europe (4.16, a), the posterior fluxes from the August inversion using only land soundings could not reduce the RMSE in concentrations, compared to the prior RMSE. However, the posterior flux from using all observations was able to reduce the RMSE slightly for the station PUI. The stations in Central/Eastern Europe (fig. 4.16, c) show RMSE concentrations, with the posterior fluxes for both August inversions, ranging from 3.6 ppm to 7.3 ppm. Some stations achieved a slight reduction in RMSE concentrations with the posterior fluxes (HUN, ZSF, HPB, KRE, JUE, WES). Overall, the difference between the RMSE concentrations from the posterior flux from August and from August all_obs is very little. For Western Europe (fig. 4.16, d) the prior and posterior RMSE concentrations were the largest for the coastal stations WAO and LUT. For the station WAO, the inversion slightly reduced the RMSE. However, this does not hold when including the ocean-soundings. For both August inversions, the RMSE could be reduced to below 10 ppm.

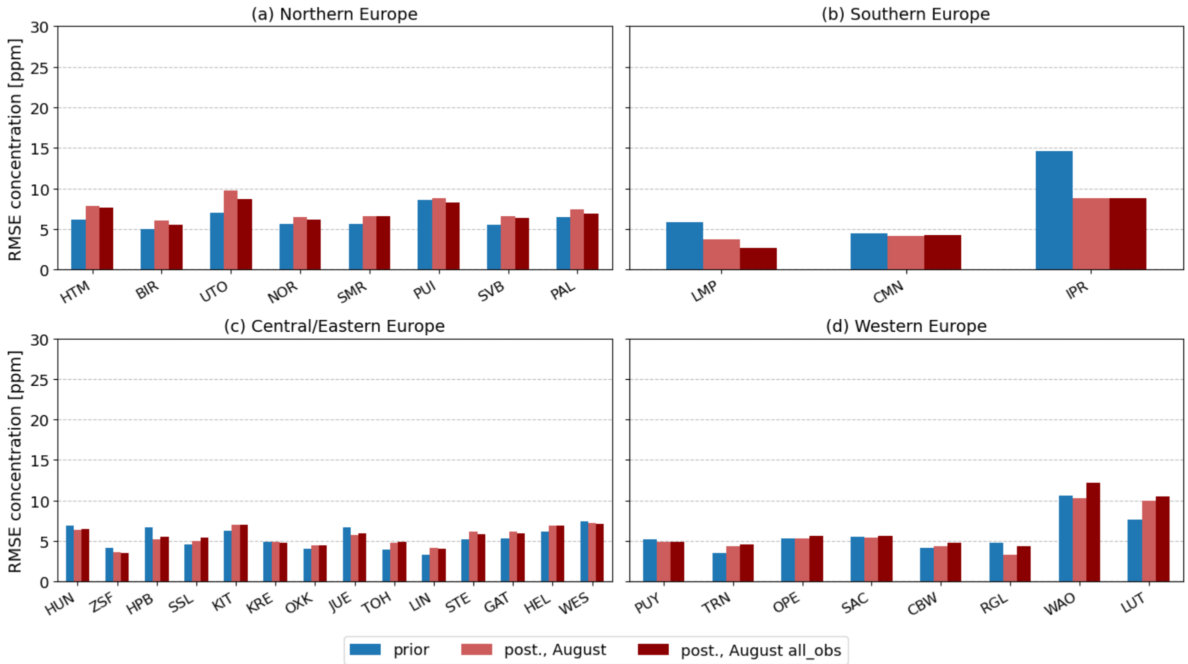


Figure 4.16: RMSE concentrations using the prior fluxes (blue) and posterior fluxes for August (light red) and August all_obs (dark red) 2022. The sites are grouped by region across Europe.

## 4.5 Sensitivity Experiments

Next, the sensitivity of the spatial and temporal correlation parameters to the posterior fluxes was tested.

### 4.5.1 Posterior biosphere fluxes for the different sensitivity cases

Figure 4.17 presents the posterior fluxes obtained from the inversions using different spatial and temporal correlation lengths. The left column shows the posterior fluxes for a spatial correlation length of 500 km, while the right column shows the results for a spatial correlation length of 100 km. Overall, a larger spatial correlation length produces spatially smoother flux patterns, whereas a smaller spatial correlation length leads to more localized patches of sources and sinks in the posterior fluxes. The influence of the temporal correlation length, comparing 7 and 30 days, is less apparent spatially, particularly for the cases with a spatial correlation length of 500 km. However, for the simulations using a spatial correlation length of 100 km, the cases with a temporal correlation length of 30 days exhibit overall stronger source and sink magnitudes compared to those using a temporal correlation length of 7 days.

### 4.5.2 Validation with ICOS observations

For the validation against the ICOS sites, the mean bias between the simulated $CO_2$ concentrations derived from the prior/posterior fluxes and the observations was calculated for all four sensitivity cases.

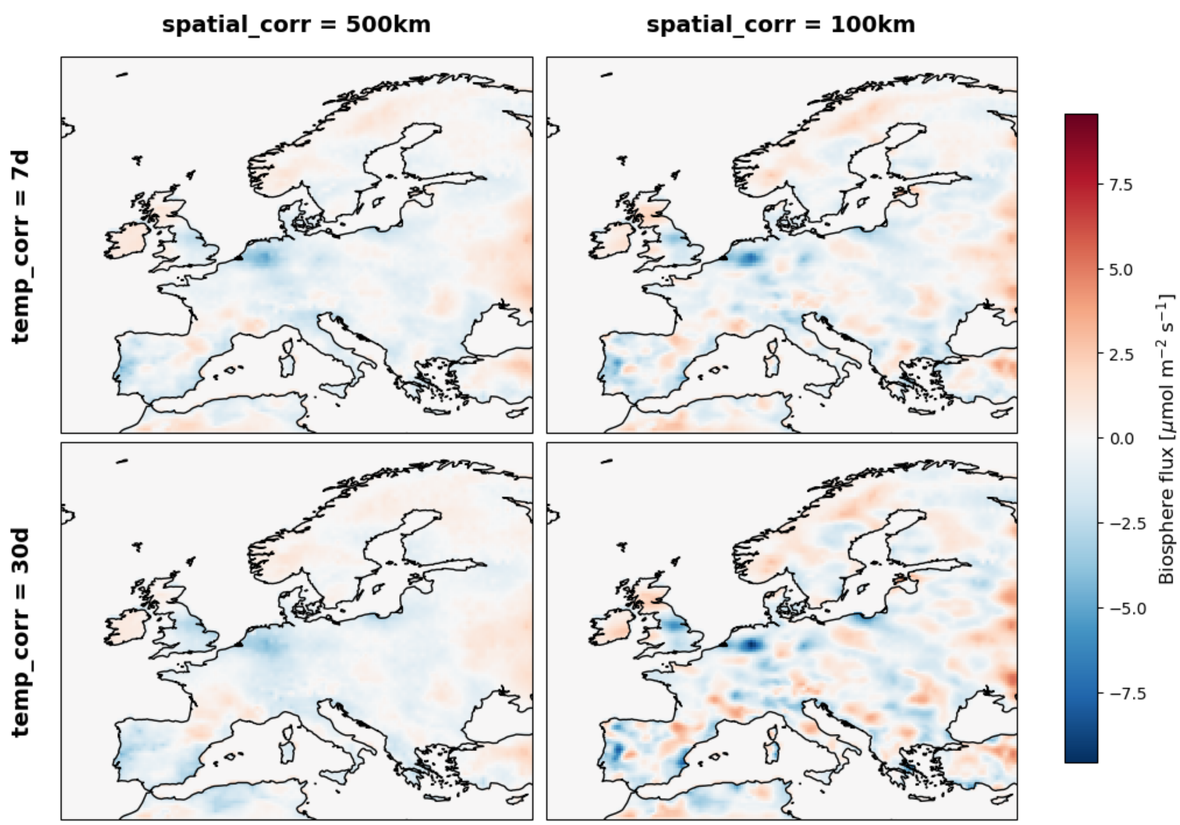


Figure 4.17: OCO-2-derived posterior flux estimates obtained using different spatial (100 km and 500 km) and temporal (7 days and 30 days) correlation length parameters.

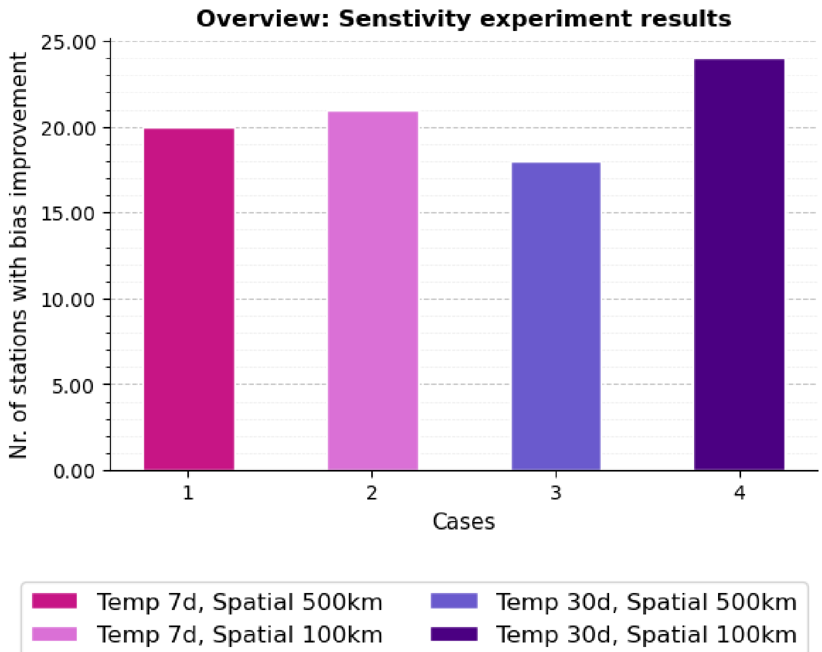


Figure 4.18: Total number of validation sites with a mean bias improvement with the posterior fluxes, displayed for each sensitivity experiment.

In terms of mean bias improvement per station, irrespective of the magnitude of the improvement, the combination of a temporal correlation length of 30 days and a spatial correlation length of 100 km produced the best results. With these correlation parameters, 24 sites across Europe showed an improved mean bias when using the posterior fluxes from the inversion. Compared to the original correlation parameters of 7 days and 500 km, this sensitivity experiment improved the results at four additional stations. The least successful combination of correlation parameters was a temporal correlation length of 30 days and a spatial correlation length of 500 km, which resulted in mean bias improvements at only 18 stations when using the posterior fluxes. Out of the eight stations in Northern Europe (fig. 4.19, a), three could achieve a bias improvement using the posterior fluxes, namely HTM, PAL and SMR. All three sites achieved a slight posterior mean bias improvement with correlation parameters of 30 days and 100 km. The magnitude of the mean bias could be reduced even more with a correlation parameter of 7 days and 100 km for the station HTM (7d, 100km: -0.67 ppm; 30d, 100km: -1.19 ppm). The remaining five stations exhibit larger posterior mean biases relative to the prior. Overall, the stations in Northern Europe show higher posterior mean biases and less improvement compared to the prior mean biases than for other regions in Europe.

Figure 4.19 (b) presents the mean biases for the three validation stations in Southern Europe, where the station IPR shows the largest prior mean bias of all stations in Europe. With using the posterior fluxes from the OCO-2 inversion, the mean bias was substantially reduced. The largest improvement, from a prior mean bias exceeding -8 ppm to a posterior mean bias close to zero, was achieved with a temporal correlation length of 30 days and a spatial correlation length of 500 km. This station also exhibits the greatest variability in posterior mean biases across the different sensitivity experiments in Southern Europe, both in magnitude and sign.

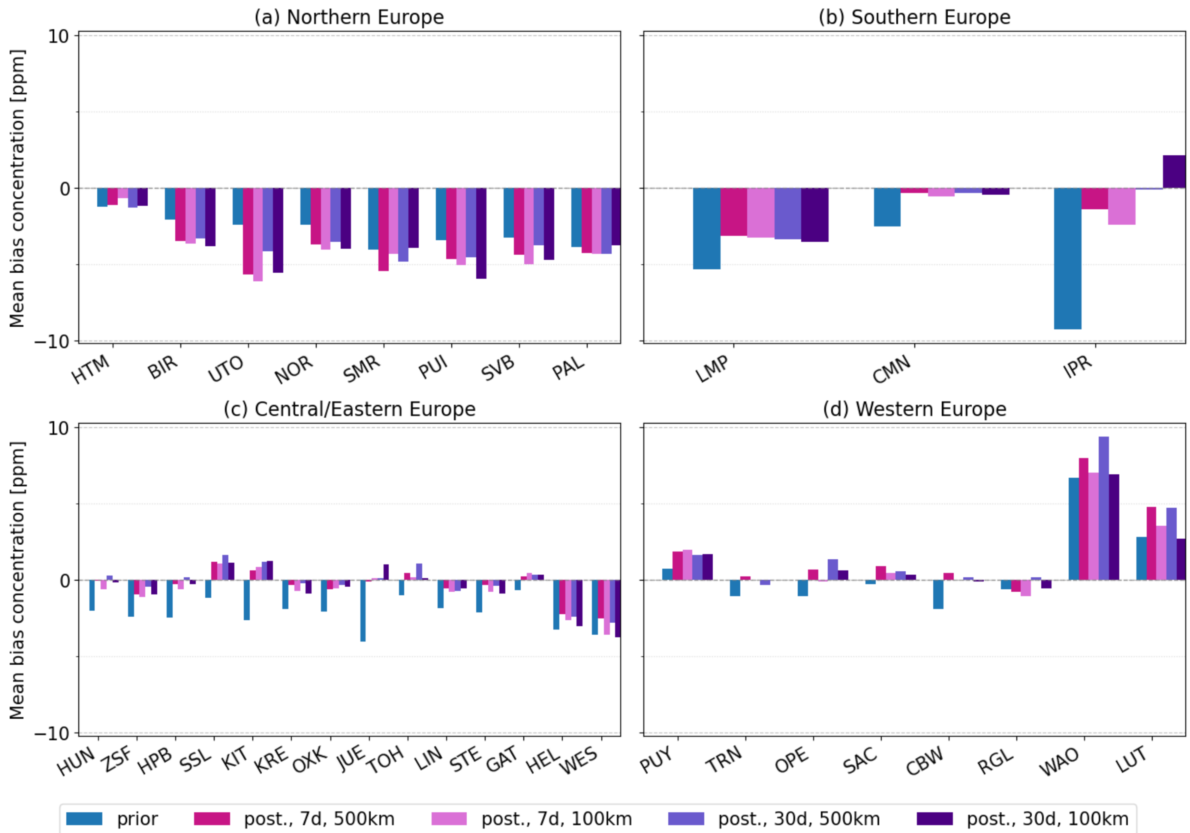


Figure 4.19: Comparison of the prior mean bias (blue) with the posterior mean bias of the different sensitivity experiments. The sites are grouped by region across Europe.

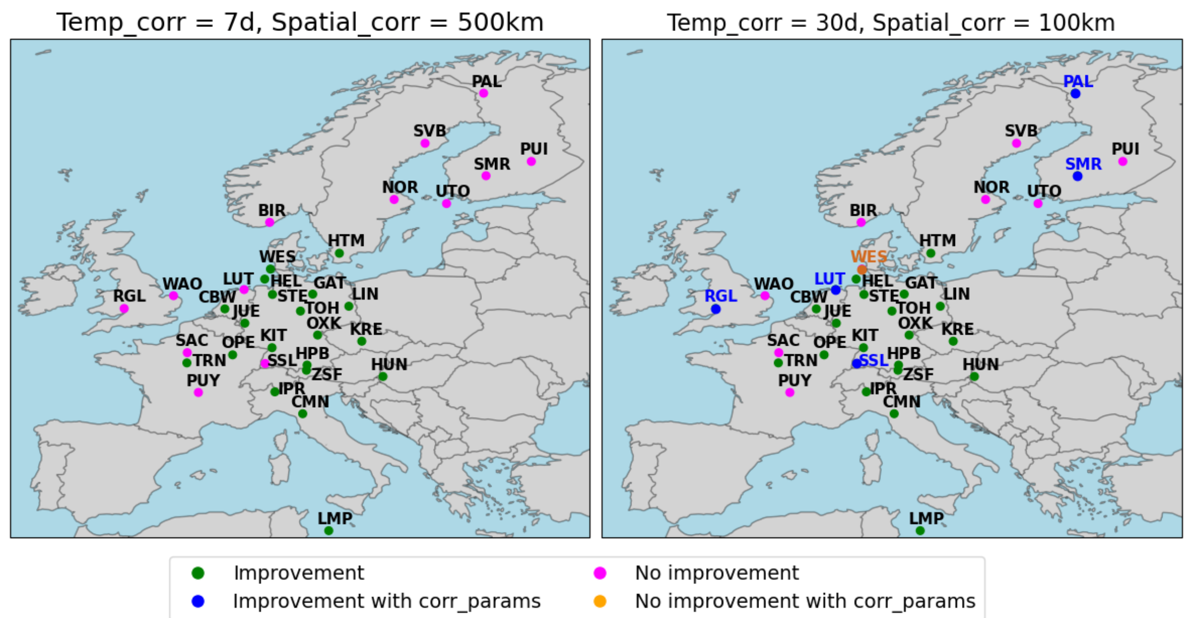


Figure 4.20: Spatial distribution of ICOS sites showing mean bias improvement (green) and no improvement (magenta) for two August inversions. In the left panel, the correlation configuration of the reference case was used (7 days, 500 km); in the right panel, the optimized correlation configuration (30 days, 100 km) was applied. Navy markers indicate stations newly improved and orange markers display stations that are not improved anymore with the optimized correlation configuration.

For the stations LMP and CMN, all four sensitivity experiments achieve a bias improvement of very similar magnitude, indicating consistent performance regardless of the correlation parameters.

Most validation sites in Central/Eastern Europe achieved a reduced mean bias with the posterior fluxes regardless of the correlation parameters (fig. 4.19, c). The exceptions are for the configuration of 30-day/500 km, for which two stations (SSL, TOH) did not show any improvement. Further, for the station WES the posterior mean bias with correlation parameters of 30 days and 100 km could not be reduced, even though prior and posterior mean biases are very similar. The station JUE exhibits the largest prior mean bias (-4.04 ppm). For this station, the inversions using correlation parameters of 7 days/500 km, 7 days/100 km and 30 days/500 km both reduced the mean bias to values close to zero. In the case of the 30 days/100 km configuration, the mean bias remained 1.0 ppm. In general, the magnitude of the posterior mean biases from different sensitivity experiments varies across the stations in Central/Eastern Europe.

For the sites in Western Europe (fig. 4.19, d), the stations WAO and LUT exhibit the largest prior mean biases (6.68 ppm and 2.82 ppm, respectively). For the coastal station LUT, only a slight reduction in mean bias was achieved and only for the correlation parameters of 30 days and 100 km. At the station WAO, the inversion was unable to improve the mean bias for any of the tested correlation parameter combinations. The posterior mean biases for this station remained high across all four sensitivity experiments, ranging from 7.02 to 9.38 ppm. In contrast, the stations TRN and CBW, which initially showed prior mean biases of -1.03 ppm and -1.92 ppm, achieved posterior mean biases close to zero for all four sensitivity cases.

Figure 4.20 shows the locations of the ICOS validation sites and indicates whether the stations achieved an improvement in mean bias when using the posterior fluxes from the OCO-2 inversion. The left panel presents the reference case of the sensitivity experiment, using a temporal correlation length of 7 days and a spatial correlation length of 500 km. The stations that achieved an improvement of the mean bias are marked in green and stations indicated with magenta showed no improvement of the mean bias with the posterior fluxes.

Following the sensitivity analysis, the combination of a temporal correlation length of 30 days and a spatial correlation length of 100 km yielded the best overall performance in terms of the number of stations showing an improvement in posterior mean bias. With this configuration, two stations in Northern Europe, two coastal stations and one station in Central Europe achieved a reduced posterior mean bias, highlighted in blue in the right panel of figure 4.20. However, the coastal site WES no longer showed an improvement in mean bias when using these correlation parameters and the corresponding posterior fluxes.

The RMSE across different sensitivity cases varies by station, more or less. The southern stations LMP and CMN (fig. 4.21, b) show only very little change in RMSE concentration across the sensitivity cases The coastal sites UTO (Northern Europe, 4.21, a) and WAO (Western Europe, fig. 4.21) display more variation in RMSE concentration across the sensitivity cases.

### 4.5.3 Validation with non ICOS sites for best correlation configuration

To test the best correlation configuration further, sites from the ObsPack dataset, that are not part of the ICOS network, were additionally used for validation purposes. The sites are spatially depicted in figure 4.23 and include multiple coastal sites. Additionally, the left panel in figure 4.23 shows the response of the mean bias when using the posterior fluxes from

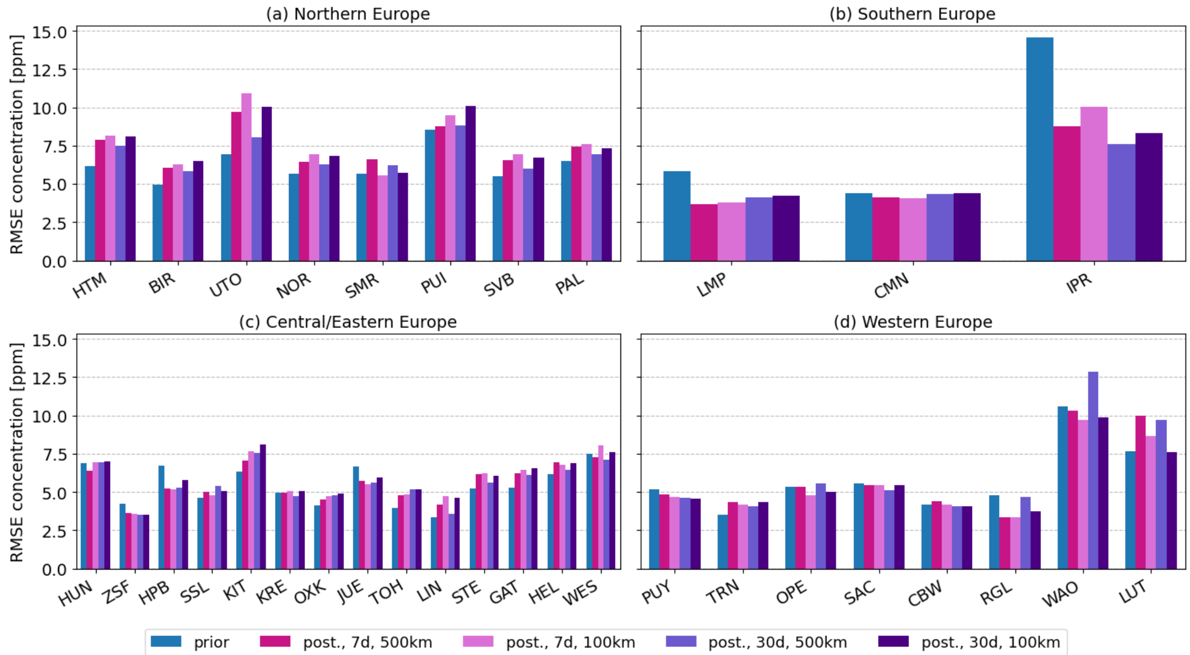


Figure 4.21: RMSE concentrations using the prior fluxes (blue) and posterior fluxes from the sensitivity experiments. The validation sites are from the ICOS observation network and are grouped by region across Europe.

the starting case, the right panel when using the optimized correlation parameters. Overall, the stations on the mainland of Europe achieved posterior mean bias reductions with both correlation configurations. However, with the optimized set of correlation parameters, no station was additionally improved. To the contrary, the posterior mean bias of the station CRA and HEI did not show an improvement anymore. Looking at the magnitude of the mean biases (fig. 4.22), the station BIS shows an outstandingly high prior as well as posterior mean bias of around -25 ppm. Both posterior fluxes were able to improve the mean bias, however, only slightly. The stations ERS, TAC and MHD showed close to zero prior mean biases. The posterior fluxes did not achieve the same small posterior mean biases, and for the station ERS the posterior mean bias was significantly higher than the prior mean bias. Figure 4.24 shows the RMSE across the non ICOS stations. Again, the station BIS shows an outstandingly high mean prediction error, indicating outliers in the observations for the month of August.

### 4.5.4 Validation with TCCON sites for best correlation configuration

Further validation of the OCO-2-derived posterior fluxes was performed using data from the TCCON sites. For August 2022, only the stations GM (Garmisch) and KA (Karlsruhe), both located in Germany, provided measurements. Posterior concentrations simulated using posterior fluxes from the reference correlation setup (7 days, 500 km) were compared with posterior concentrations simulated using posterior fluxes obtained with the optimized correlation parameters of 30 days and 100 km.
Figure 4.25 shows that simulations using posterior fluxes with the optimized correlation parameters substantially reduced both the mean bias and the RMSE. At station GM, reductions

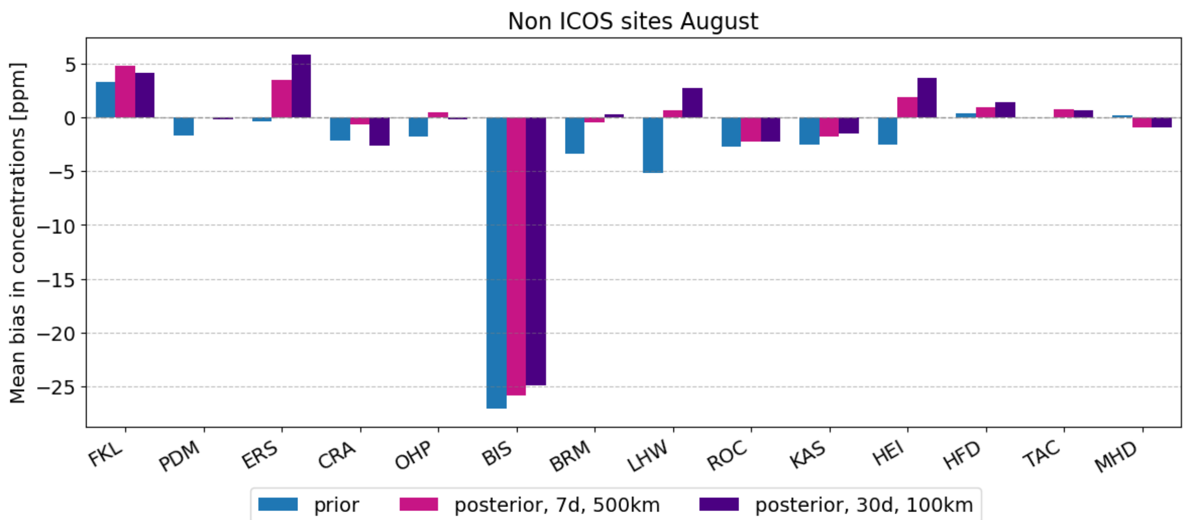


Figure 4.22: Comparison of the prior mean bias (blue) with the posterior mean biases for non ICOS stations, for OCO-2-derived posterior fluxes with the correlation parameters of 7 days/500km (pink) and 30 days/100km (purple).

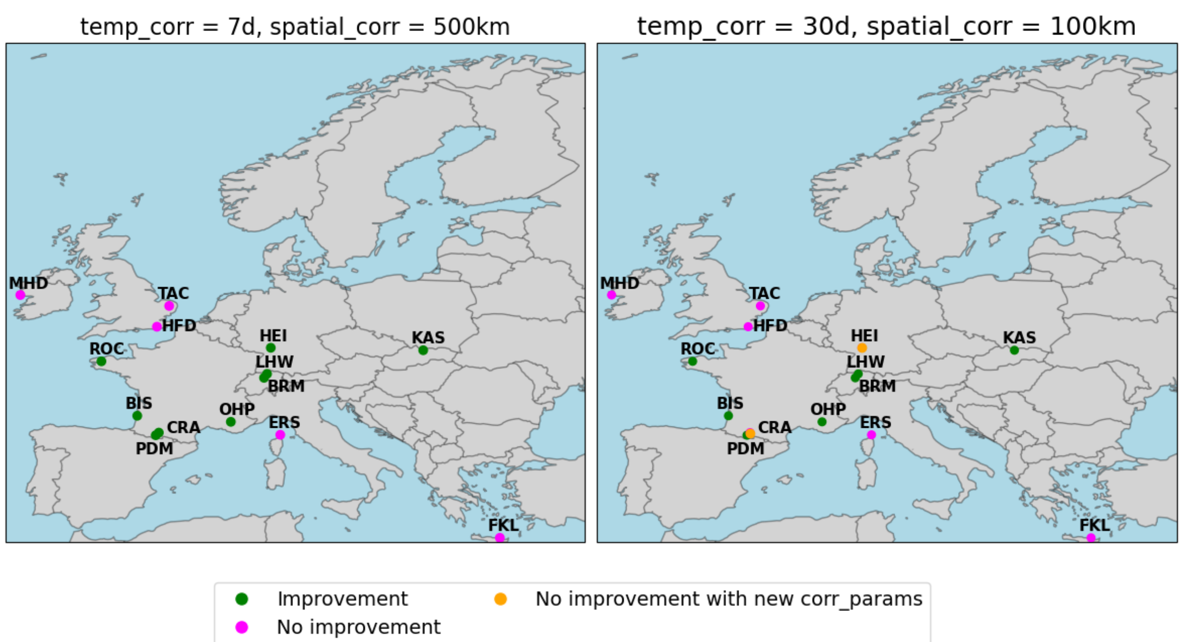


Figure 4.23: Spatial distribution of non ICOS sites showing mean bias improvement (green) and no improvement (magenta) for two August inversions. In the left panel, the correlation configuration of the reference case was used (7 days, 500km), in the right panel the optimized correlation configuration (30 days, 100km) was applied. The orange markers display stations that are no longer improved with the optimized correlation configuration.

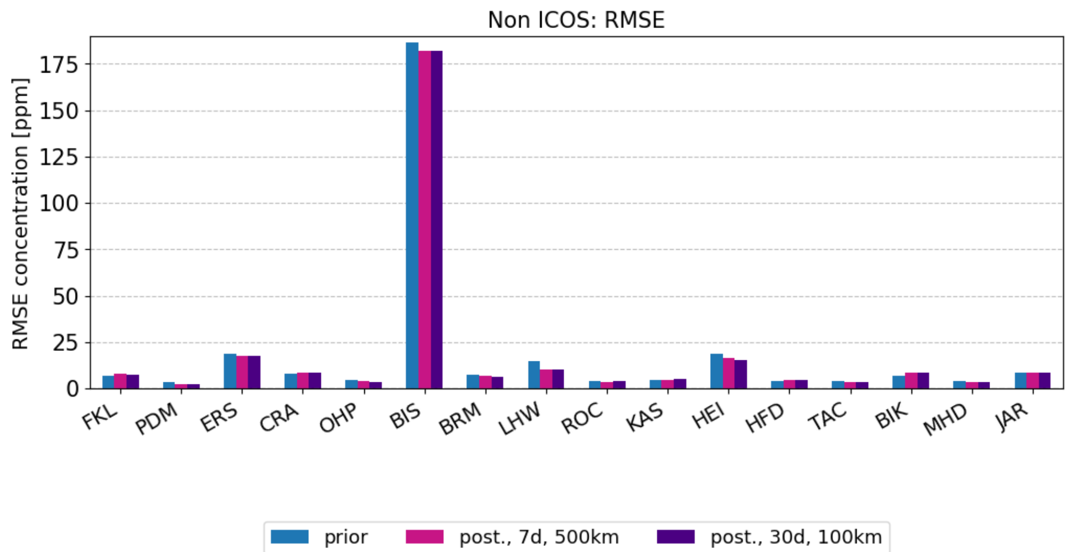


Figure 4.24: RMSE concentrations for the non ICOS validation sites with the prior fluxes (blue) and the posterior fluxes for the reference case (7 days, 500km) displayed in pink and the optimized correlation parameters (30 days, 100km) shown in purple.

in posterior mean bias and RMSE were achieved only when using the optimized correlation parameters. At station KA, the prior mean bias of 77.46 ppm was reduced to 13.07 ppm when using posterior fluxes derived with the 30 days and 100 km correlation parameters (fig. 4.25, a).

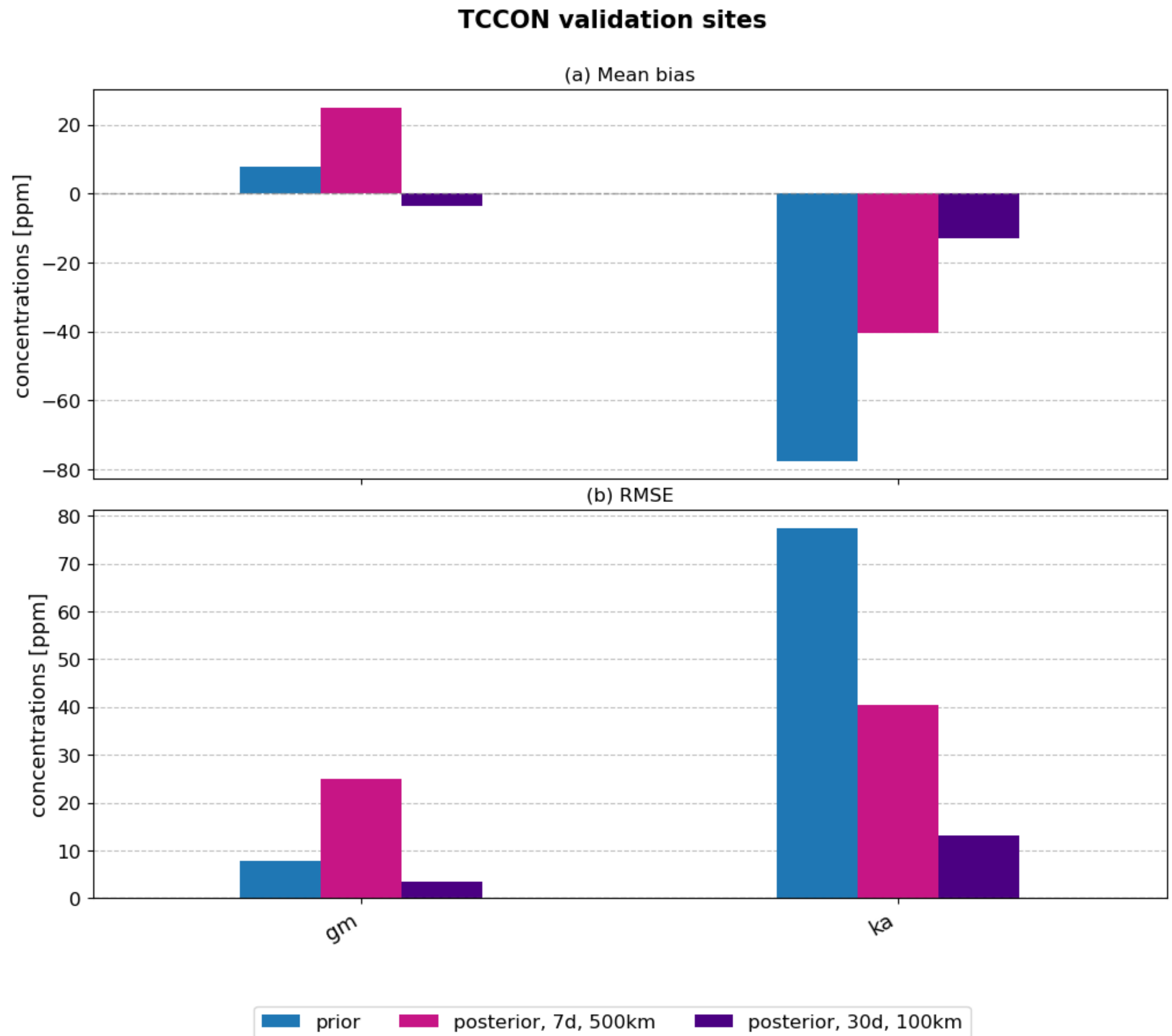


Figure 4.25: Comparison of prior (blue) and posterior concentrations with observations at the TCCON sites. The upper panel presents the mean bias, and the lower panel shows the RMSE. The OCO-2-derived posterior fluxes are based on correlation parameters for the reference case (7 days/500 km) displayed in pink and with the optimized correlation configuration of 30 days/100 km shown in purple.

# Chapter 5

# Discussion

## 5.1 Simulated $CO_2$ vs. OCO-2 observations

The simulated $CO_2$ concentrations using prior fluxes from LPJ-GUESS exhibited high variability not captured in the OCO-2 observations. Since the background concentrations show only limited variability, most of the spread likely originates from the foreground contribution. As explained in section 2.1.2, the foreground contribution is the scalar product of sounding-specific footprints and the surface fluxes. Hence, moderate emission sensitivities, combined with an increased prior mix of surface fluxes, can lead to high simulated concentrations. In August, fire activity in southwestern France (Lanet et al. 2024) led to increased prior surface fluxes and peak concentrations exceeding 600 ppm. In January, the high variability in simulated concentrations is driven by greater variability in the biosphere and anthropogenic flux components.

Furthermore, since there is no ground truth available for the footprints, validating the results is challenging. Nevertheless, the validation against the ICOS, non-ICOS and TCCON sites still showed a reduction in posterior mean bias for many stations, suggesting that the results remain promising despite the high variability in the simulated concentrations with prior fluxes.

After obtaining the OCO-2-derived posterior fluxes and using them to simulate the $CO_2$ concentrations, the agreement with the OCO-2 observations markedly improved. The improvement is especially pronounced in January, where the variability of the simulated concentrations decreases substantially, leading to a closer match between the simulated concentrations and the observed values. This outlines the capability of the OCO-2-derived posterior fluxes to improve the agreement with the OCO-2 observations.

## 5.2 Comparison of prior and posterior biosphere fluxes

The prior from LPJ-GUESS indicated more carbon sources throughout Europe for January and August, whereas the OCO-2 posterior fluxes depicted large parts of Europe as carbon sinks.

Previous studies (Houweling et al. 2015; Reuter et al. 2014) using GOSAT satellite data and different inversion systems have suggested that the European carbon sink is larger than inferred from in situ measurements. However, the findings of Crowell et al. (2019) contradict this conclusion, reporting similar annual carbon sinks regardless of whether satellite or in situ observations were used as observational constraints. Furthermore, Feng et al. (2016) identified biases in the GOSAT retrievals as a potential explanation for the large European carbon sink estimated by several inversion systems.

Peiro et al. (2022) conducted an intercomparison study, assimilating the bias-corrected OCO-2 v.9 retrievals, OCO-2 v.7 retrievals and in situ observations as a baseline to compare the obtained results. Their findings showed that version 9 produced larger summertime carbon sinks over Europe and, notably, exhibited better agreement with the findings of Houweling et al. (2015) than version 7. They further argued that version 9 appears to be more consistent with previous studies (e.g. Houweling et al. (2015), Reuter et al. (2014)). Nevertheless, Peiro et al. (2022) emphasized that further analysis is required to understand the origin of the differences between versions 7 and 9 over Europe.

The present study uses OCO-2 retrievals from version 11.2, which have been shown to exhibit improved bias characteristics compared with earlier versions (Das et al. 2025). However, the literature continues to highlight the sensitivity of inversion results to retrieval biases and how such biases can propagate through inversion systems, potentially leading to erroneous estimates of $CO_2$ fluxes. This underscores the importance of continued efforts to reduce biases in satellite retrievals. In addition, Chevallier et al. (2014) emphasized that uncertainties in prior fluxes, systematic retrieval errors, and transport model inaccuracies all reduce confidence in posterior flux estimates.

Moreover, posterior flux estimates are strongly influenced by both the observational density and the spatial distribution of the soundings in January and August. Consequently, sparse observational coverage yields weak constraints on the fluxes and therefore reduces the reliability of the posterior estimates. Since central/northern Europe exhibited only very limited to no soundings in January, the posterior fluxes in these regions are not very trustworthy. In contrast, the posterior fluxes for August are constrained by a larger number of observations, particularly over Central Europe, resulting in more reliable estimates that also show better agreement with the posterior fluxes derived from ICOS observations. This is also consistent with the findings of Crowell et al. (2019), who report in their model intercomparison study assimilating OCO-2 and in situ observations that agreement between in situ- and satellite-derived fluxes is primarily achieved in regions where both observation types are dense enough to provide sufficient observational constraint.

## 5.3 Influence of observational density on the inversion results

Comparing the validation results for January and August (land-soundings) underlined the importance of a high observational coverage to improve mean biases with the posterior fluxes. In January, the posterior fluxes were unable to reduce the mean biases for most validation sites on the mainland of Europe. This is due to the low observational density in the vicinity of the stations. However, despite the lack of observations in Northern Europe, apart from a few super-observations in the southernmost part of Sweden, northern validation sites still improved by the posterior fluxes of the inversion. This may seem surprising, as there is little observational information to constrain the prior fluxes directly. However, the inversion accounts for both spatial and temporal correlation lengths when finding the best set of fluxes to fit the observations. This is likely the main reason for the observed improvements in posterior mean bias. Consequently, even relatively small discrepancies in the magnitude of the prior mean bias could already be classified as improvements in the posterior mean bias.

For the sites in northern Italy (PRS, IPR, CMN), the posterior fluxes were not able to improve the mean bias, even though there were observations in the close vicinity of the stations. However, for CMN and PRS, the magnitude of the prior and posterior mean bias is very similar, indicating also no degradation in accuracy. The site IPR, on the other hand, showed the overall largest prior and posterior mean biases, as well as the largest RMSE concentrations across all validation sites. This underlines that the posterior flux estimates for this site are very uncertain. Having a closer look at the location of the site reveals that it lies in the close surroundings (~30 km radius) of several mountains with altitudes up to 2200 m. PRS and CMN are also both mountain sites at an altitude of 3480 m and 2165 m. This complex terrain affects transport model simulations, as local topographic flows and boundary layer characteristics must be represented accurately in the transport model, which can be challenging (Madala et al. 2015). Further, the accuracy of the OCO-2 observations is influenced by complex topography. As shown by Jacobs et al. (2024), the digital elevation model used in the retrieval process plays an important role in determining observation accuracy, which in turn affects inversion results.

Overall, including the ocean soundings in the August inversion had little influence on the mean posterior bias. Given the increased observational density near the coastal validation sites, a positive effect on reducing the posterior mean bias could have been expected. This held true for two stations in proximity to the ocean, which showed reduced posterior mean bias. Interestingly, three stations in Western/Central Europe were even negatively influenced by the ocean soundings, with a slightly higher posterior mean bias than the prior mean bias. Having a closer look at the super-observations for August all_obs shows additional observations mainly in France, likely due to inland water bodies that are accounted for in ocean glint mode. Furthermore, while OCO-2 version 11 exhibits improved accuracy for ocean glint soundings, the biases remain higher than those for land-based observations (Das et al. 2025). This could explain the slight increase in posterior mean biases for the stations in France and at the border to France, when including the ocean-soundings in the inversion.

## 5.4 Sensitivity experiments to find the best correlation configuration

The temporal and spatial resolutions of the ICOS and satellite-based observations differ substantially. While ICOS provides hourly $CO_2$ observations at a network of sites across Europe, OCO-2 offers near-global coverage of 16 days, resulting in high spatial coverage in the domain but limited temporal resolution. Consequently, the optimal configuration of correlation parameters for the OCO-2 inversions differed from those derived for the ICOS-based inversions.

In terms of the number of validation stations showing an improvement in mean bias with the posterior fluxes, the ideal temporal correlation length was 30 days with a spatial correlation length of 100 km. With the reduced spatial correlation length, more localized carbon sinks and sources throughout Europe emerged, which is an expected behavior.

In general, the influence of the correlation parameters on the single sites varies a lot. Depending on the validation station, different sets of correlation parameters achieved the largest posterior mean bias reduction. In contrast to the results for January, the station IPR achieved a large mean bias reduction of 9.4 ppm with the ideal correlation parameters of 30 days and 500 km for this station. In this particular case, the correlation configurations with a spatial correlation length of 500 km achieved a larger mean bias reduction. A reason for that could be the increased observational density in August in the radius of 500 km compared to January. However, even though the RMSE was reduced at that site with the posterior fluxes, it still remained high (around 7.5 ppm for all sensitivity cases), which indicates a large mean error of the predictions. For the stations in Central/Easter Europe, all stations except for SSL and TOH showed an improved posterior mean bias, regardless of the correlation parameters. Identifying the best set of correlation parameters for these stations, therefore, remains challenging, as the magnitude of the posterior mean bias varies depending on the different sites. For the two coastal sites WAO (England) and LUT (the Netherlands), the large prior mean biases remained, showing no mean bias reduction with the posterior fluxes. Only for the correlation parameters of 30 days and 100 km, a slight improvement was seen for the station LUT. The lacking ability of reducing the posterior mean bias was also depicted for the stations in Northern Europe, where the prior fluxes seemed to be a more accurate representation than the posterior fluxes. Thompson et al. (2025) point out that the air masses in the columns of the satellite column observations have more diverse sources compared to point observations. This again leads to a more spread-out Source-Receptor-Relationship (SRR) for satellite observations and a weaker constraint of each individual retrieval on the fluxes. Hence, many more retrievals are needed to accomplish a similar constraint as given by point observations. This applies to any region but has a larger effect at higher latitudes because of the naturally lower observational density, driven by fewer sun hours during winter months, enhanced cloud cover, and optically thick aerosols that perturb OCO-2 observations. This could therefore be a possible reason for the lack of ability to improve the posterior mean biases in northern Europe.

The non-ICOS validation sites obtained from Obspack showed no improvement of results with the optimized correlation parameters, in terms of the number of stations with a reduced posterior mean bias. To the contrary, the original correlation settings of 7 days and 500 km showed better results. The exceptionally high mean bias and RMSE concentrations at the station BIS were investigated further and are most likely attributable to wildfire activity occurring near the station during August 2022 (Lanet et al. 2024).

Validation against the two TCCON sites showed that the high prior mean biases and RMSE values of the simulated concentrations were reduced when using the posterior fluxes. The optimized correlation parameter configuration achieved the largest reduction at both sites, whereas the correlation parameters of 7 days and 500 km did not reduce posterior mean biases or RMSE with the posterior fluxes. For the Karlsruhe station, both ICOS and TCCON observations are available. As observed in the ICOS validation, the posterior mean bias was lower than in the TCCON-based validation. This difference could be attributable to gaps in the TCCON observations during August, as measurements were not consistently available between 12:00 and 13:00 at either station each day. In addition, the differing observation types affect the validation results, as TCCON measures total-column-averaged concentrations, whereas ICOS provides point measurements of $CO_2$. The total-column observations may reflect contributions from different source regions at different altitudes within the atmospheric column, this again will be reflected in the total-column footprints, which are used for the validation.

## 5.5 Limitations and future extensions

The lack of observations in the northern parts of Europe limits the potential for improving mean biases with the posterior fluxes in these regions. In addition, OCO-2 column-averaged observations are generally less accurate than in situ or TCCON observations (Das et al. 2025).

Unlike OCO-2, the ground-based total-column measurements provided by TCCON are unaffected by surface properties and only minimally sensitive to aerosols and high cirrus clouds (Keppel-Aleks et al. 2007). ICOS observations, which consist of point measurements of $CO_2$, are not affected by these issues. Consequently, the lower accuracy of the OCO-2 observations, compared to in situ and TCCON observations, further limits the accuracy of inversion results derived from OCO-2 flux estimates.

The three-step averaging scheme applied to the observations in this study substantially reduced the number of available observations. Although this is not optimal, calculating footprints for every individual observation would be computationally very expensive. Furthermore, the observational gaps in the TCCON data limit the reliability of the validation of the OCO-2-derived posterior fluxes.

Moreover, a wider range of spatial correlation lengths could be explored in future studies, including values both smaller and larger than 100 km. This could be an interesting extension in examining the influence of additional spatial correlation parameters. Further, the spatial distribution of simulated concentrations based on prior fluxes could be investigated further to determine whether specific regions in Europe are primarily responsible for the high variability.

Su et al. (2024) and Liu et al. (2024) demonstrate in their studies that the joint incorporation of in situ and satellite $CO_2$ observations yields better results in terms of RMSE than only using a single source for the data assimilation. However, this is challenging because the heterogeneity of observations from different sources must be properly accounted for (Su et al. 2024). Although these studies employed inversion systems different from the one used in this project, this approach could provide a promising direction for extending the current work and further reducing RMSE values.

# Chapter 6

# Conclusion

This study demonstrated the simulation of total-column footprints with FLEXPART v.11 for satellite observations from OCO-2 (version 11.2). The main challenge of using total-column retrievals with Lagrangian transport models is the large amount of observations that need to be averaged effectively to reduce the computational cost and make simulations realizable. To maintain as much variability of the data as possible, super-observations were formed with an adaptive grid cell averaging scheme. After a successful implementation, the setup was tested with the regional inversion system LUMIA for the months of January and August 2022. For August, the inclusion of ocean retrievals as well as the effect of different sets of correlation parameters was explored.
Resulting from that, two research questions were posed:

1. How well do simulated $CO_2$ concentrations, using OCO-2 total-column retrievals and prior fluxes derived from land surface models, match OCO-2 observations?

2. To what extent are biases in OCO-2-derived posterior concentration fields reduced against TCCON column retrievals and ground-based in situ observations?

While the OCO-2 observations lie within the range of simulated concentrations with the prior fluxes from LPJ-GUESS, the variability of the simulated concentrations was high. The source of the variability was determined to come from more spread-out satellite footprints and the prior fluxes. As the foreground contributions result from the scalar product of the footprints with the prior fluxes, peak values in surface fluxes, e.g., from wildfire activity, can lead to a high variability in simulated concentrations. In contrast to that, the background concentrations acquired from CAMS show a stable trend over time.
The lack of observational density in January led to fewer stations that achieved a mean bias reduction with the posterior fluxes. For August, a large number of stations in Central/Eastern Europe were able to reduce the mean bias with the posterior fluxes. The inclusion of the ocean soundings in the August inversion only improved two sites that are in the vicinity of the sea and had a negative effect on three stations inland. It therefore did not prove to be helpful to include the ocean soundings in the inversion.
The best set of correlation parameters revealed to be a temporal correlation length of 30 days and a spatial correlation length of 100 km. This was determined based on the number of stations that achieved a mean bias reduction with the posterior fluxes, not considering the magnitude of the reduction. The best correlation configurations in terms of reduction of

posterior mean bias magnitude depended very much on the location site. A wider range of spatial correlation lengths could be explored, as this correlation parameter appears to have the greatest impact on the results. Validation using the TCCON sites showed that gaps in the observational record, together with differences in observation type, resulted in higher posterior mean biases and RMSE values compared with those obtained at the same validation location within the ICOS network.

The errors were measured by the RMSE metric. While posterior fluxes mostly reduced the concentration in RMSE across the validation sites in Europe, the RMSE concentrations still remained high, ranging from 3.5 ppm to 12.8 ppm, depending on the site and correlation set. However, none of the northern stations reduced the RMSE concentrations with the posterior fluxes. The attribution of errors could have several sources. Generally, a higher error with satellite observations can be expected. As explained by (Thompson et al. 2025), this could be due to the fact that column observations have more diverse sources of air masses compared to point observations. This leads to a more spread-out SRR and a weaker constraint on fluxes, compared to point observations. In fact, total-column observations may even reflect contributions from different source regions at different altitudes within the atmospheric column, making their interpretation and application in inversion systems more challenging. Especially in higher latitudes, this effect amplifies as the observational network is scarcer in general. The exceptionally high RMSE for the station BIS can be explained by surrounding wildfire activities during the observational period.

This study provides a valuable contribution toward utilizing the increasing availability of satellite-based observations and exploring the new capabilities of FLEXPART 11, which enable the integration of total-column data into the transport model. Future extensions of this work could be the joint assimilation of in situ and total-column observations, an approach that has shown promising results and has achieved greater reductions in RMSE than the use of a single observational data source (Su et al. (2024); Liu et al. (2024)).

# Chapter 7

# Appendix

Table 7.1: Non-ICOS sites and TCCON sites: station codes and full station names.

| **Station code** | **Station name** | **Dataset** |
|---|---|---|
| FKL | Finokalia | non-ICOS |
| PDM | Pic du Midi | non-ICOS |
| ERS | Ersa | non-ICOS |
| CRA | Centre de Recherches Atmosphériques | non-ICOS |
| OHP | Observatoire de Haute Provence | non-ICOS |
| BIS | Biscarrosse | non-ICOS |
| BRM | Beromunster | non-ICOS |
| LHW | Laegern-Hochwacht | non-ICOS |
| ROC | Roc'h Trédudon | non-ICOS |
| KAS | Kasprowy Wierch | non-ICOS |
| HEI | Heidelberg | non-ICOS |
| HFD | Heathfield | non-ICOS |
| TAC | Tacolneston | non-ICOS |
| BIK | Bialystok | non-ICOS |
| MHD | Mace Head | non-ICOS |
| JAR | Järvselja | non-ICOS |
| gm | Garmisch | TCCON |
| ka | Karlsruhe | TCCON |

Table 7.2: ICOS sites: station codes and full station names

| **Station code** | **Station name** |
|---|---|
| LMP | Lampedusa |
| CMN | Monte Cimone |
| PUY | Puy de Dôme |
| IPR | Ispra |
| PRS | Plateau Rosa |
| HUN | Hegyhátsál háttérszennyettség-mérő állomás |
| ZSF | Zugspitze |
| HPB | Hohenpeissenberg |
| SSL | Schauinsland |
| TRN | Trainou |
| OPE | Observatoire pérenne de l'environnement |
| SAC | Saclay |
| KIT | Karlsruhe |
| KRE | Křešín u Pacova |
| OXK | Ochsenkopf |
| JUE | Jülich |
| TOH | Torfhaus |
| CBW | Cabauw |
| RGL | Ridge Hill |
| LIN | Lindenberg |
| WAO | Weybourne |
| STE | Steinkimmen |
| GAT | Gartow |
| LUT | Lutjewad |
| HEL | Helgoland |
| WES | Westerland |
| HTM | Hyltemossa |
| BIR | Birkenes |
| UTO | Utö - Baltic Sea |
| NOR | Norunda |
| SMR | Hyytiälä |
| PUI | Puijo |
| SVB | Svartberget |
| PAL | Pallas |

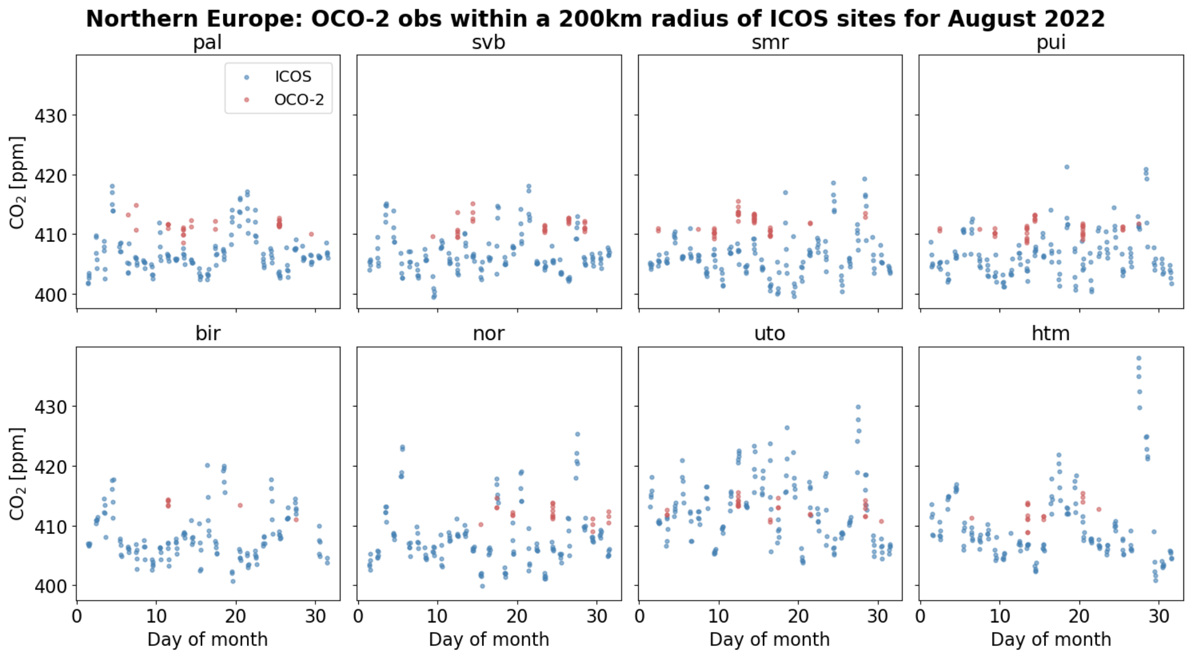


Figure 7.1: ICOS observations (blue) and OCO-2 observations (red) within 200 km of the respective ICOS site, displayed are the sites in Northern Europe for August 2022.

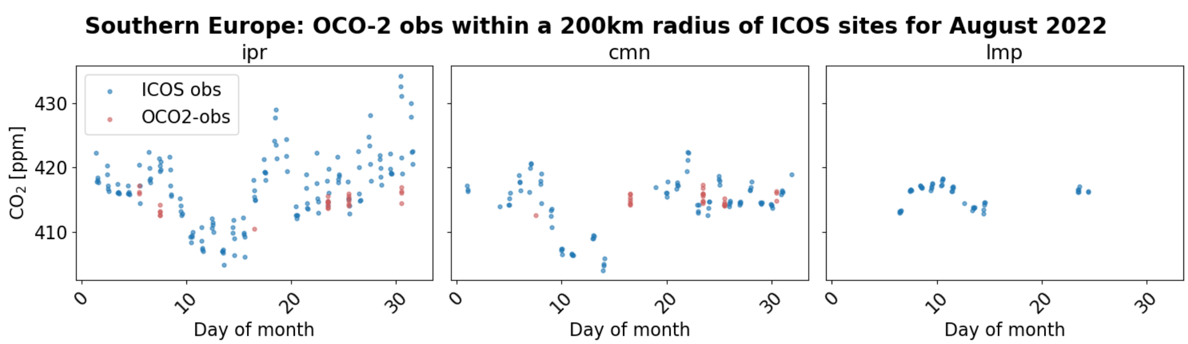


Figure 7.2: ICOS observations (blue) and OCO-2 observations (red) within 200 km of the respective ICOS site, displayed are the sites in Southern Europe for August 2022.

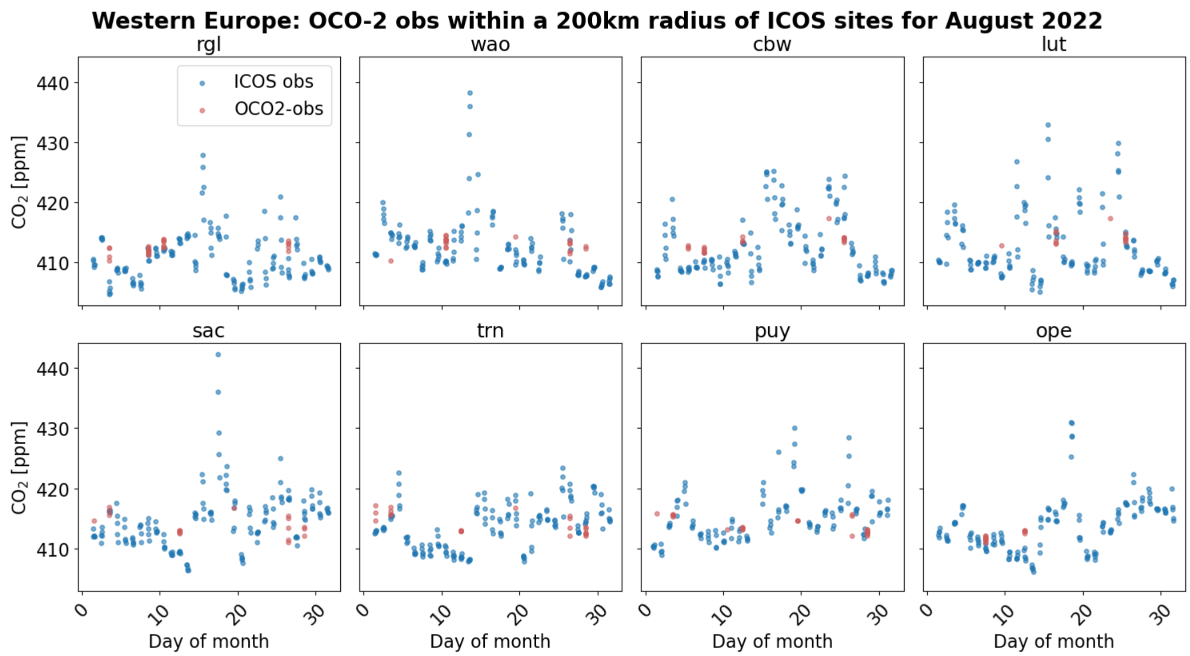


Figure 7.3: ICOS observations (blue) and OCO-2 observations (red) within 200 km of the respective ICOS site, displayed are the sites in Western Europe for August 2022.

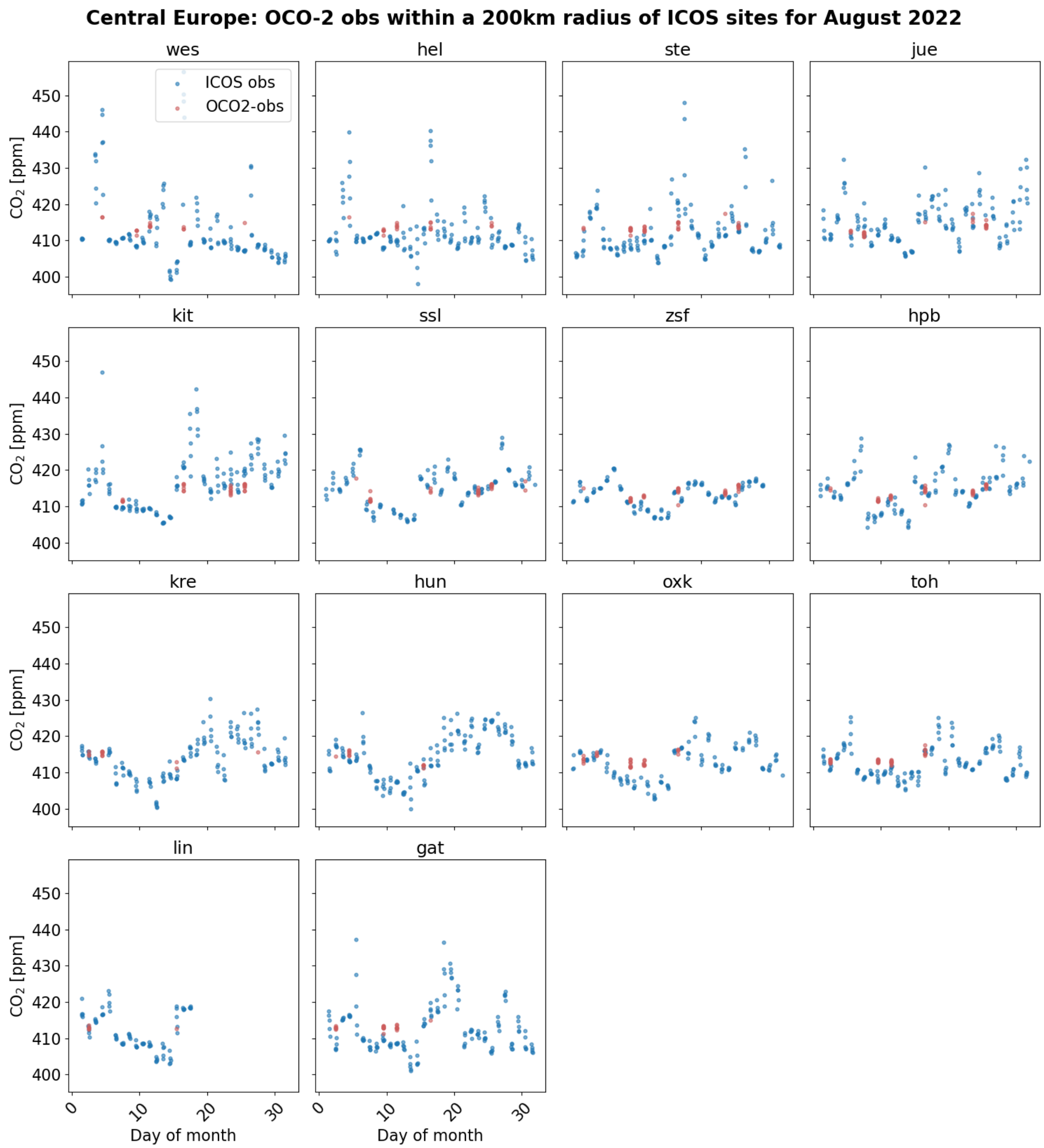


Figure 7.4: ICOS observations (blue) and OCO-2 observations (red) within 200 km of the respective ICOS site, displayed are the sites in Central/Eastern Europe for August 2022.

# Bibliography


Arias, P., et al., 2021: Technical summary. *Climate Change 2021: The Physical Science Basis. Contribution of Working Group I to the Sixth Assessment Report of the Intergovernmental Panel on Climate Change*, V. Masson-Delmotte, P. Zhai, A. Pirani, S. Connors, C. Péan, S. Berger, N. Caud, Y. Chen, L. Goldfarb, M. Gomis, M. Huang, K. Leitzell, E. Lonnoy, J. Matthews, T. Maycock, T. Waterfield, O. Yeleçi, R. Yu, und B. Zhou, Eds., Cambridge University Press, Cambridge, United Kingdom and New York, NY, USA, 33–144, https://doi.org/10.1017/9781009157896.002.

Bakels, L., D. Tatsii, A. Tipka, R. Thompson, M. Dütsch, M. Blaschek, P. Seibert, K. Baier, S. Bucci, M. Cassiani, S. Eckhardt, C. G. Zwaaftink, S. Henne, P. Kaufmann, V. Lechner, C. Maurer, M. D. Mulder, I. Pisso, A. Plach, R. Subramanian, M. Vojta, und A. Stohl, 2024: FLEXPART version 11: improved accuracy, efficiency, and flexibility. *Geoscientific Model Development*, **17 (21)**, 7595–7627, https://doi.org/10.5194/gmd-17-7595-2024.

Chatterjee, A., und A. M. Michalak, 2013: Technical note: Comparison of ensemble kalman filter and variational approaches for co2 data assimilation. *Atmospheric Chemistry and Physics*, **13**, 11 643–11 660, https://doi.org/10.5194/ACP-13-11643-2013.

Chevallier, F., P. I. Palmer, L. Feng, H. Boesch, C. W. O'Dell, und P. Bousquet, 2014: Toward robust and consistent regional co 2 flux estimates from in situ and spaceborne measurements of atmospheric co 2. *Geophysical Research Letters*, **41**, 1065–1070, https://doi.org/10.1002/2013GL058772.

Connor, B. J., H. Boesch, G. Toon, B. Sen, C. Miller, und D. Crisp, 2008: Orbiting Carbon Observatory : Inverse method and prospective error analysis. *Journal Geophysical Research*, **113**, 1–14, https://doi.org/10.1029/2006JD008336.

Crisp, D., 2008: The orbiting carbon observatory: Nasa's first dedicated carbon dioxide mission. *Sensors, Systems, and Next-Generation Satellites XII*, SPIE, Proceedings of SPIE, Vol. 7106, https://doi.org/10.1117/12.802194.

Crisp, D., A. Eldering, B. Drouin, J. Laughner, G. Mcgarragh, B. Connor, I. Polonski, M. Smyth, und D. Thompson, 2021: Oco-2 level 2 full physics retrieval algorithm theoretical basis.

Crowell, S., D. Baker, A. Schuh, S. Basu, A. R. Jacobson, F. Chevallier, J. Liu, F. Deng, L. Feng, K. Mckain, A. Chatterjee, J. B. Miller, B. B. Stephens, A. Eldering, D. Crisp, D. Schimel, R. Nassar, C. W. O'dell, T. Oda, C. Sweeney, P. I. Palmer, und D. B. A. Jones, 2019: The 2015-2016 carbon cycle as seen from oco-2 and the global in situ network. *Atmos. Chem. Phys*, **19**, 9797–9831, https://doi.org/10.5194/acp-19-9797-2019.

Das, S., M. Kiel, J. Laughner, G. Osterman, C. W. O'Dell, T. E. Taylor, B. Fisher, F. Chevallier, N. M. Deutscher, M. K. Dubey, D. G. Feist, O. Garcia, D. W. Griffith, F. Hase, L. T. Iraci, R. Kivi, I. Morino, J. Notholt, H. Ohyama, D. Pollard, S. Roche, C. M. Roehl, C. Rousogenous, M. K. Sha, K. Shiomi, K. Strong, R. Sussmann, T. Yao, G. Toon, M. Vrekoussis, P. Wang, T. Warneke, P. Wennberg, A. Chatterjee, V. H. Payne, und D. Wunch, 2025: Comparisons of the v11.1 orbiting carbon observatory-2 (oco-2) xco2 measurements with ggg2020 tccon. *Earth and Space Science*, **12**, https://doi.org/10.1029/2024EA003935.

Feng, L., P. I. Palmer, R. J. Parker, N. M. Deutscher, D. G. Feist, R. Kivi, I. Morino, und R. Sussmann, 2016: Estimates of european uptake of co 2 inferred from gosat x co 2 retrievals: sensitivity to measurement bias inside and outside europe. *Atmospheric Chemistry and Physics*, **16**, 1289–1302, https://doi.org/10.5194/acp-16-1289-2016.

Fortems-Cheiney, A., I. Pison, G. Dufour, G. Broquet, L. Costantino, A. Fortems-Cheiney, I. Pison, G. Dufour, G. Broquet, L. Costantino, Fortems-Cheiney, A., Pison, I., Dufour, G., Broquet, G., Costantino, und L., 2017: Regional inverse modeling for high reactive species with pyvar-chimere. *AGUFM*, **2017**, A33A–2339.

Friedlingstein, P., et al., 2026: Global carbon budget 2025. *Earth Syst. Sci. Data*, **18**, 3211–3288, https://doi.org/10.5194/essd-18-3211-2026.

Ganesan, A. L., M. Rigby, M. F. Lunt, R. J. Parker, H. Boesch, N. Goulding, T. Umezawa, A. Zahn, A. Chatterjee, R. G. Prinn, Y. K. Tiwari, M. V. D. Schoot, und P. B. Krummel, 2017: Atmospheric observations show accurate reporting and little growth in india's methane emissions. *Nature Communications*, **8**, https://doi.org/10.1038/s41467-017-00994-7.

Gurney, K. R., R. M. Law, A. S. Denning, P. Rayner, D. Baker, P. Bousquet, L. Bruhwiler, Y.-H. Chen, P. Ciais, und S. Fan, 2002: Towards robust regional estimates of co2 sources and sinks using atmospheric transport models. *Nature*, **415**, 626–630, https://doi.org/10.1038/415626a.

Hersbach, H., et al., 2020: The ERA5 global reanalysis. *Quarterly Journal of the Royal Meteorological Society*, **146 (730)**, 1999–2049, https://doi.org/10.1002/qj.3803.

Houweling, S., D. Baker, S. Basu, H. Boesch, A. Butz, F. Chevallier, F. Deng, E. J. Dlugokencky, L. Feng, A. Ganshin, O. Hasekamp, D. Jones, S. Maksyutov, J. Marshall, T. Oda, C. W. O'Dell, S. Oshchepkov, P. I. Palmer, P. Peylin, Z. Poussi, F. Reum, H. Takagi, Y. Yoshida, und R. Zhuravlev, 2015: An intercomparison of inversemodels for estimating sources and sinks of co2 using gosat measurements. *Journal of Geophysical Research*, **120**, 5253–5266, https://doi.org/10.1002/2014JD022962.

Huijnen, V., J. Williams, M. V. Weele, T. V. Noije, M. Krol, F. Dentener, A. Segers, und S. Houweling, 2010: Model Development The global chemistry transport model TM5: description and evaluation of the tropospheric chemistry version 3.0. *Geoscientific Model Development*, **3**, 445–473, https://doi.org/10.5194/gmd-3-445-2010.

ICOS Research Infrastructure, 2018: ICOS Near Real-Time (Level 1) Atmospheric Greenhouse Gas Mole Fractions of CO2, CO and CH4, growing time series starting from latest Level 2 release. ICOS ERIC, https://doi.org/10.18160/ATM_NRT_CO2_CH4.

Jacobs, N., C. W. O'Dell, T. E. Taylor, T. L. Logan, B. Byrne, M. Kiel, R. Kivi, P. Heikkinen, A. Merrelli, V. H. Payne, und A. Chatterjee, 2024: The importance of digital elevation model accuracy in xco2 retrievals: Improving the orbiting carbon observatory 2 atmospheric carbon observations from space version 11 retrieval product. *Atmospheric Measurement Techniques*, **17**, 1375–1401, https://doi.org/10.5194/AMT-17-1375-2024.

Keppel-Aleks, G., G. C. Toon, P. O. Wennberg, und N. M. Deutscher, 2007: Reducing the impact of source brightness fluctuations on spectra obtained by fourier-transform spectrometry. *Applied Optics, Vol. 46, Issue 21, pp. 4774-4779*, **46**, 4774–4779, https://doi.org/10.1364/AO.46.004774.

Konovalov, I. B., N. A. Golovushkin, und E. A. Mareev, 2025: Using oco-2 observations to constrain regional co2 fluxes estimated with the vegetation, photosynthesis and respiration model. *Remote Sensing*, **17**, 177, https://doi.org/10.3390/RS17020177/S1.

Lanet, M., L. Li, A. Ehret, S. Turquety, und H. L. Treut, 2024: Attribution of summer 2022 extreme wildfire season in southwest france to anthropogenic climate change. *npj Climate and Atmospheric Science*, **7**, https://doi.org/10.1038/s41612-024-00821-z.

Liu, S., X. Pan, X. Xiong, T. Sun, L. Xue, H. Zhang, J. Fang, J. Fang, G. Zhang, H. Xu, und B. Chen, 2024: Integration of surface-based and space-based atmospheric co2 measurements for improving carbon flux estimates using a new developed 3-gas inversion model. *Atmospheric Research*, **307**, 107 477, https://doi.org/10.1016/J.ATMOSRES.2024.107477.

Madala, S., A. N. Satyanarayana, und C. V. Srinivas, 2015: Simulation of atmospheric dispersion of nox over complex terrain region of ranchi with flexpart-wrf by incorporation of improved turbulence intensity relationships. *Atmospheric Environment*, **123**, 139–155, https://doi.org/10.1016/J.ATMOSENV.2015.10.090.

Masarie, K. A., W. Peters, A. R. Jacobson, und P. P. Tans, 2014: Obspack: a framework for the preparation, delivery, and attribution of atmospheric greenhouse gas measurements. *Earth Syst. Sci. Data*, **6**, 375–384, https://doi.org/10.5194/essd-6-375-2014.

Monteil, G., und M. Scholze, 2021: Regional CO 2 inversions with LUMIA , the Lund University Modular Inversion Algorithm , v1 . 0. *Geoscientific Model Development*, **14 (6)**, 3383–3406, https://doi.org/10.5194/gmd-14-3383-2021.

OCO-2/OCO-3 Science Team, Vivienne Payne, und Abhishek Chatterjee, 2024: Oco-2 level 2 bias-corrected xco2 and other select fields from the full-physics retrieval aggregated as daily files, retrospective processing v11.2r. Goddard Earth Sciences Data and Information Services Center (GES DISC), Greenbelt, MD, USA, https://doi.org/10.5067/70K2B2W8MNGY.

O'Dell, C. W., et al., 2018: Improved retrievals of carbon dioxide from orbiting carbon observatory-2 with the version 8 acos algorithm. *Atmospheric Measurement Techniques*, **11**, 6539–6576, https://doi.org/10.5194/AMT-11-6539-2018.

Peiro, H., S. Crowell, A. Schuh, D. F. Baker, C. O'Dell, A. R. Jacobson, F. Chevallier, J. Liu, A. Eldering, D. Crisp, F. Deng, B. Weir, S. Basu, M. S. Johnson, S. Philip, und I. Baker, 2022: Four years of global carbon cycle observed from the orbiting carbon observatory 2 (oco-2) version 9 and in situ data and comparison to oco-2 version 7. *Atmospheric Chemistry and Physics*, **22**, 1097–1130, https://doi.org/10.5194/ACP-22-1097-2022.

Peylin, P., R. M. Law, K. R. Gurney, F. Chevallier, A. R. Jacobson, T. Maki, Y. Niwa, P. K. Patra, W. Peters, P. J. Rayner, C. Rödenbeck, I. T. V. D. Laan-Luijkx, und X. Zhang, 2013: Global atmospheric carbon budget: Results from an ensemble of atmospheric co2 inversions. *Biogeosciences*, **10**, 6699–6720, https://doi.org/10.5194/BG-10-6699-2013.

Pisso, I., E. Sollum, H. Grythe, N. I. Kristiansen, M. Cassiani, S. Eckhardt, D. Arnold, D. Morton, R. L. Thompson, C. D. G. Zwaaftink, N. Evangeliou, H. Sodemann, L. Haimberger, S. Henne, D. Brunner, J. F. Burkhart, A. Fouilloux, J. Brioude, A. Philipp, P. Seibert, und A. Stohl, 2019: The lagrangian particle dispersion model flexpart version 10.4. *Geoscientific Model Development*, **12**, 4955–4997, https://doi.org/10.5194/GMD-12-4955-2019.

Reithmeier, B. C., und R. Sausen, 2002: ATTILA: atmospheric tracer transport in a Lagrangian model. *Tellus*, **54 (3)**, 278–299, https://doi.org/10.3402/tellusb.v54i3.16666.

Reuter, M., M. Buchwitz, M. Hilker, J. Heymann, O. Schneising, D. Pillai, H. Bovensmann, J. P. Burrows, H. Bösch, R. Parker, A. Butz, O. Hasekamp, C. W. O'Dell, Y. Yoshida, C. Gerbig, T. Nehrkorn, N. M. Deutscher, T. Warneke, J. Notholt, F. Hase, R. Kivi, R. Sussmann, T. Machida, H. Matsueda, und Y. Sawa, 2014: Satellite-inferred european carbon sink larger than expected. *Atmospheric Chemistry and Physics*, **14**, 13 739–13 753, https://doi.org/10.5194/ACP-14-13739-2014.

Seibert, P., und A. Frank, 2004: Source-receptor matrix calculation with a Lagrangian particle dispersion model in backward mode. *Atmospheric Chemistry and Physics*, **4 (1)**, 51–63.

Sitch, S., P. Friedlingstein, N. Gruber, S. Jones, G. Murray-Tortarolo, A. Ahlström, S. Doney, H. Graven, C. Heinze, C. Huntingford, S. Levis, P. Levy, M. Lomas, B. Poulter, N. Viovy, S. Zaehle, N. Zeng, A. Arneth, G. Bonan, L. Bopp, J. Canadell, F. Chevallier, P. Ciais, R. Ellis, M. Gloor, P. Peylin, S. Piao, C. Le Quéré, B. Smith, Z. Zhu, und R. Myneni, 2015: Recent trends and drivers of regional sources and sinks of carbon dioxide. *Biogeosciences*, **12**, 653–679, https://doi.org/10.5194/bg-12-653-2015.

Smith, B., I. C. Prentice, und M. T. Sykes, 2001: Representation of vegetation dynamics in the modelling of terrestrial ecosystems: comparing two contrasting approaches within european climate space. *Global Ecology and Biogeography*, **10 (6)**, 621–637, https://doi.org/10.1046/j.1466-822X.2001.t01-1-00256.x.

Stohl, A., C. Forster, A. Frank, P. Seibert, und G. Wotawa, 2005: Technical note: The Lagrangian particle dispersion model. *Atmospheric Chemistry and Physics*, **5**, 2461–2474, https://doi.org/10.5194/acp-5-2461-2005.

Su, W., B. Wang, H. Chen, L. Zhu, X. Zheng, und S. X. Chen, 2024: A new global carbon flux estimation methodology by assimilation of both in situ and satellite co2 observations. *npj Climate and Atmospheric Science 2024 7:1*, **7**, 287–, https://doi.org/10.1038/s41612-024-00824-w.

Sussmann, R., M. Rettinger, und N. Mostafavi Pak, 2025: Tccon data from garmisch (de), release ggg2020.r1. CaltechDATA, https://doi.org/10.14291/tccon.ggg2020.garmisch01.R1.

Thompson, R. L., N. Krishnankutty, I. Pisso, P. Schneider, und K. Stebel, 2025: Efficient use of a Lagrangian particle dispersion model for atmospheric inversions using satellite observations of column mixing ratios. *Atmospheric Chemistry and Physics*, **25 (19)**, 12 737–12 751, https://doi.org/10.5194/acp-25-12737-2025.

Thompson, R. L., und A. Stohl, 2014: Flexinvert: An atmospheric bayesian inversion framework for determining surface fluxes of trace species using an optimized grid. *Geoscientific Model Development*, **7**, 2223–2242, https://doi.org/10.5194/GMD-7-2223-2014.

Van der Gon, H. D., 2023: D2.2 prior emission data 2021 documentation. Tech. rep.

Varon, D. J., D. J. Jacob, B. Hmiel, R. Gautam, D. R. Lyon, M. Omara, M. Sulprizio, L. Shen, D. Pendergrass, H. Nesser, Z. Qu, Z. R. Barkley, N. L. Miles, S. J. Richardson, K. J. Davis, S. Pandey, X. Lu, A. Lorente, T. Borsdorff, J. D. Maasakkers, und I. Aben, 2023: Continuous weekly monitoring of methane emissions from the permian basin by inversion of tropomi satellite observations. *Atmospheric Chemistry and Physics*, **23**, 7503–7520, https://doi.org/10.5194/ACP-23-7503-2023.

Villalobos, Y., P. J. Rayner, J. D. Silver, S. Thomas, V. Haverd, J. Knauer, Z. M. Loh, N. M. Deutscher, D. W. Griffith, und D. F. Pollard, 2021: Was australia a sink or source of $CO_2$ in 2015? Data assimilation using OCO-2 satellite measurements. *Atmospheric Chemistry and Physics*, **21**, 17 453–17 494, https://doi.org/10.5194/acp-21-17453-2021.

Villalobos, Y., C. Gómez-Ortiz, M. Scholze, G. Monteil, U. Karstens, A. Fiore, D. Brunner, J. Thanwerdas, und P. Cristofanelli, 2025: Towards improving top-down national $CO_2$ estimation in Europe: potential from expanding the icos atmospheric network in italy. *Environmental Research Letters*, **20**, https://doi.org/10.1088/1748-9326/adc41e.

Wu, D., J. C. Lin, B. Fasoli, T. Oda, X. Ye, T. Lauvaux, E. G. Yang, und E. A. Kort, 2018: A Lagrangian approach towards extracting signals of urban CO 2 emissions from satellite observations of atmospheric column $CO_2$ ($XCO_2$): X-Stochastic Time-Inverted Lagrangian Transport model (" X-STILT v1 "). *Geoscientific Model Development*, **11 (12)**, 4843–4871, https://doi.org/10.5194/gmd-11-4843-2018.

Wunch, D., G. C. Toon, J.-F. L. Blavier, R. A. Washenfelder, J. Notholt, B. J. Connor, D. W. T. Griffith, V. Sherlock, und P. O. Wennberg, 2011: The total carbon column observing network. *Trans. R. Soc. A*, **369**, 2087–2112, https://doi.org/10.1098/rsta.2010.0240.

Zhang, Q., M. Li, C. Wei, A. P. Mizzi, Y. Huang, und Q. Gu, 2021: Assimilation of oco-2 retrievals with wrf-chem/dart: A case study for the midwestern united states. *Atmospheric Environment*, **246**, 118 106, https://doi.org/10.1016/J.ATMOSENV.2020.118106.

Master’s Theses in Mathematical Sciences 2026:E66
ISSN 1404-6342

LUNFBV-3014-2026

Computational Science
Centre for Mathematical Sciences
Lund University
Box 118, SE-221 00 Lund, Sweden

http://www.maths.lu.se/